

Controlled synthesis and characterization of porous silicon nanoparticles for dynamic nuclear polarization

Gevin von Witte,^{†,‡} Aaron Himmler,[‡] Viivi Hyppönen,[¶] Jiri Jäntti,[§] Mohammed M. Albannay,[†] Jani O. Moilanen,^{||} Matthias Ernst,[‡] Vesa-Pekka Lehto,[§] Joakim Riikonen,[§] Sebastian Kozerke,[†] Mikko I. Kettunen,^{¶,⊥} and Konstantin Tamarov^{*,§,⊥}

[†]*Institute for Biomedical Engineering, University and ETH Zurich, Zurich, Switzerland*

[‡]*Institute of Molecular Physical Science, ETH Zurich, Zurich, Switzerland*

[¶]*Kuopio Biomedical Imaging Unit, A.I. Virtanen Institute, University of Eastern Finland, Kuopio, Finland*

[§]*Department of Technical Physics, University of Eastern Finland, Kuopio, Finland*

^{||}*Department of Chemistry, Nanoscience Center, University of Jyväskylä, Jyväskylä, Finland*

[⊥]*Joint senior authorship*

E-mail: konstantin.tamarov@uef.fi

Abstract

Si nanoparticles (NPs) have been actively developed as a hyperpolarized magnetic resonance imaging (MRI) agent with an imaging window of more than one hour. However, the progress in the development of NPs has been hampered by the incomplete

understanding of their structural properties that correspond to efficient hyperpolarization build up and long polarization decays. In this work we study dynamic nuclear polarization (DNP) of single crystal porous Si (PSi) NPs with defined doping densities ranging from nominally undoped to highly doped with boron or phosphorus. To develop such PSi NPs we perform low-load metal-assisted catalytic etching for electronic grade Si powder followed by thermal oxidation to form the dangling bonds in the Si/SiO₂ interface, the P_b centers, which are the endogenous source of the unpaired electron spins necessary for DNP. The controlled fabrication and oxidation procedures allow us to thoroughly investigate the impact of the magnetic field, temperature and doping on the DNP process, as well as to identify the rate limiting step for the polarization buildup and decay. We argue that the buildup and decay rate constants are limited by the polarization transfer across the nuclear spin diffusion barrier determined by the large hyperfine shift of the central ²⁹Si nuclei of the P_b centers. Finally, we find the room temperature relaxation of low boron doped PSi NPs reaching 75 ± 3 minutes and nuclear polarization levels exceeding $\sim 6\%$ when polarized at 6.7 T and 1.4 K. Our study thus establishes solid grounds for further development of Si NPs.

Introduction

Magnetic resonance imaging (MRI) is a non-invasive versatile technique that provides anatomical images with sub-millimeter spatial¹ and milliseconds time² resolutions. Applying recent advances in artificial intelligence based image reconstruction and enhancement methods,³ low field MRI has recently reached real world adoption even in the mobile setting.⁴ MRI, however, is inherently insensitive at room temperature due to low thermal polarization of nuclei, which complicates the observation of nuclei other than ¹H. Detecting low-abundant nuclei, such as ¹³C, ¹⁵N or ²⁹Si, brings additional versatility to MRI allowing to *e.g.*, image tumor metabolism,⁵ locally detect pH,^{6,7} detect Si particles *in-vivo* within prolonged time window.⁸⁻¹⁰ Porous Si nanoparticles (NPs) hold particular promise due to their biocompat-

ibility and numerous treatment modalities.¹¹

To detect Si NPs in an MRI scanner, their ^{29}Si nuclei require hyperpolarization *i.e.*, a polarization significantly beyond thermal equilibrium value at the body temperature. A mature method to hyperpolarize various nuclei in the solid state is dynamic nuclear polarization (DNP).¹² DNP requires the presence of polarized unpaired electronic spins, whose polarization is subsequently transferred to hyperfine (HF) coupled nuclei by (near-) resonant microwave (MW) irradiation.

In Si, the unbound electrons required for DNP can originate from substitutional donor dopant atoms, such as group V (P, As, Sb, Bi) or group VI (S) atoms, which carry one or more donor electrons. As each dopant carries extra electron(s), the majority carriers are negatively charged electrons and Si is named *n*-type. Spins of electrons bound to ^{31}P donors has been widely used to polarize ^{29}Si nuclear spins and to study polarization dynamics in bulk Si samples with different ^{29}Si and ^{31}P content.¹³⁻¹⁶ Polarization enhancement comparable to the theoretical maximum limits of γ_e/γ_n (the gyromagnetic ratios of electrons and nuclei) have been obtained when ^{29}Si content was purified to 1.3%.¹³ Importantly, nuclear spin diffusion (nSD), a process that equalizes the nuclear spin polarization between distant ^{29}Si , was found to be relatively independent from the P doping density despite the strong hyperfine (HF) shifts in ^{29}Si Larmor frequencies.¹³ Doping density, however, affects the mechanism of polarization transfer from electrons to ^{29}Si nuclei. With the variation of ^{31}P and ^{29}Si content, well resolved solid effect (SE),^{13,15,16} differential SE¹³ and Overhauser effect (OE)¹⁴⁻¹⁶ DNP mechanisms of ^{29}Si hyperpolarization have been identified. Finally, more sophisticated protocols, such as resonant polarization transfer from polarized ^{31}P to ^{29}Si nuclei,¹⁷ have been demonstrated.

If Si is doped with group III atoms, in particular boron, each dopant atom binds an electron leaving a hole in the valence band. The majority carriers are the positively charged holes and the Si is called *p*-type. Hole states in the valence band form from the *p*-orbitals as opposed to the *s*-orbitals for the conduction band. The need to satisfy the 3-fold degen-

eracy of the p -orbital results in the splitting of the valence band into the heavy and light hole bands.¹⁸ The degeneracy of these bands combined with the dopant atom-induced local random stresses broadens the electron paramagnetic resonance (EPR) spectrum making it hard to observe in B-doped Si unless uniaxial strain is applied.^{19–21} Strained single crystal Si:B has been used to study the integrated solid effect.²⁰

Another source of electron spins are defect sites found in amorphous Si,²² oxidized Si surfaces^{23–25} and elemental Si particles.^{8,9,26} Such defect sites are characterized by a broken Si bond with an unpaired electron mostly localized on the central Si atom.²⁵ When the defect is located at the Si/SiO₂ interface, it is called the P_b center.^{23–25} P_b centers and P_b -like centers in amorphous Si have been used to hyperpolarize various Si particles and applied them as background-free contrast agents for MRI.^{8,27} The long spin-lattice (T_{1n}) relaxation times of Si particles around ~ 40 min at room temperature offered extended imaging time windows compared to about 30 s in ¹³C molecules⁶ or 145 s (15 min) in nanodiamonds (microdiamonds).²⁸ In diamonds, the substitutional nitrogen defects in the particle’s bulk (often called C or P1 center) are responsible for the DNP while surface dangling bonds commonly cause strong relaxation. The surface dangling bonds thus are detrimental for nanodiamonds with high surface-to-bulk ratio leading to lower polarization levels and faster relaxation compared to microdiamonds.²⁹ This is different from the case in Si with the P_b centers located on the interface to the naturally forming surface oxide which allow the polarization of 50 nm particles.²⁶

Despite the demonstrated high nuclear polarization and long nuclear T_{1n} relaxation times at room temperature^{26,30} in the bulk Si particles, the underlying reasons to observe long T_{1n} remain unclear. The diversity of fabrication methods further complicates the identification of the structural properties, their comparison between the different particles and influence on T_{1n} . In this study, we apply top-down fabrication approach^{31,32} to produce porous silicon nanoparticles (PSi NPs) with high surface area from doping controlled, single crystal Si wafers. The role of the high surface area is twofold. First, it enables the controlled formation

of relatively large number of endogenous P_b centers to drive the DNP process. To the best of our knowledge, previous attempts to hyperpolarize PSi NPs required the use of external radicals for DNP to be efficient,¹⁰ complicating possible MRI applications of those NPs. Second, large surface area combines good biocompatibility with a well understood diverse chemistry for (targeted) nanocarrier capabilities¹¹ making the PSi NPs suitable both for imaging and drug delivery.¹¹ Herein, we prove that endogenous P_b centers in PSi NPs are capable of providing the DNP enhancements similar to state-of-the-art bulk particles.²⁶ We, furthermore, demonstrate that specific doping level of the crystalline pore walls increase the room temperature T_{1n} relaxation time to more than one hour, which is almost twice superior compared to the previous data.

Results

Previous studies on the DNP of Si NPs relied on either commercially available^{9,26,30,33} or on in-house bottom-up fabrication approaches.^{10,30,34,35} In contrast, we selected single crystal Si wafers as the starting material to precisely control crystallinity and doping level (Table 1). In addition to wafers, we tested a relatively cheaper commercially available polycrystalline Si powder with known concentration of impurities (MC10 sample). The wafers were fractured in a planetary ball mill to obtain a 10–25 μm dry powder before gold (Au)-catalyzed low-load metal-assisted catalytic etching (LL-MACE) was employed to form a porous powder.³²

The porous powder was then thermally oxidized^{39,40} to form the surface oxide and to introduce the P_b centers in the Si/SiO₂ interface. In the last step, a dedicated low speed small milling system⁴¹ was used to fracture the porous silicon from micrometer- to nanometer-sized particles and to avoid excessive forces that could lead to dislocations and, therefore, paramagnetic centers inside the Si crystals. More details about the NP fabrication can be found in the Experimental section. The final Si NPs possessed irregular shapes and average sizes of 150 ± 65 nm (Fig. 1a,b). Additional milling and centrifugal post-milling selection

Table 1: Summary of Si grade abbreviations used to fabricate PSi NPs.

Abbreviation	Resistivity ($\Omega \cdot \text{cm}$)	Dopant	Doping density (cm^{-3}) ^a	Average dopant distance (nm) ^b
P++ ^c	0.0186	Boron	$4 \cdot 10^{18}$	3.49
P+ ^c	0.105	Boron	$3 \cdot 10^{17}$	8.27
P ^c	25	Boron	$5 \cdot 10^{14}$	69.8
UW ^c	> 5000	Boron	< 10^{12}	> 554
N ^c	19.7	Phosphorus	$2.3 \cdot 10^{14}$	90.4
N+ ^c	1.15	Phosphorus	$3 \cdot 10^{15}$	38.4
N++ ^c	0.0144	Phosphorus	$3 \cdot 10^{18}$	3.84
MC10 ^d	Metallurgical grade powder, polycrystalline, 99.997% purity. Impurities: Al, Fe, Ca, Ti			

^a Dopant densities were calculated using Caughey-Thomas expression³⁶ for electron and hole mobilities. Effective Bohr radii are 1.3 (3.8) and 2.1 nm for heavy (light) holes and electrons in B doped and P doped Si, respectively. The effective Bohr radius of the P electron assumes the pancake-like wavefunction ansatz proposed by Kohn and Luttinger.³⁷ ^b Average distance between the dopant atoms was calculated from their density using the random probability distribution in three dimensions;³⁸ ^c Powder from single crystal (100) wafers, Okmetic; ^d Elkem Silicon Products.

can further decrease the average size if required by *e.g.*, a specific biological or medical application.

LL-MACE resulted in etch track pores (> 10 nm) produced by Au NPs boring into Si and tortuous pores (< 10 nm) (Fig. 1c) produced by hole escape from space-charge layers to distant Si surfaces.^{31,32} This porosity was a necessary prerequisite to obtain high specific surface area and pore volume which determined high number of surface P_b centers after oxidation. X-ray powder diffraction (Fig. 1e and Sec. ??, Suppl. Inf.) demonstrated the presence of two distinct Si peaks. Since the Si particles are single crystal before etching (except for the MC10 sample) and preserve the crystallinity during the etch, the peaks corresponded to the pore voids according to the Babinet's principle.⁴² The narrower XRD peaks (30 – 60 nm bars) were thus attributed to the etch track pores, while the wider ones (5 – 10 nm bars) were due to tortuous pores penetrating the large crystals (Fig. 1e).^{31,32} The wide and narrow XRD peaks were on the order of the corresponding pore sizes measured by N₂ sorption and depicted in Fig. 1c. The catalytic Au NPs were also clearly present in the Si

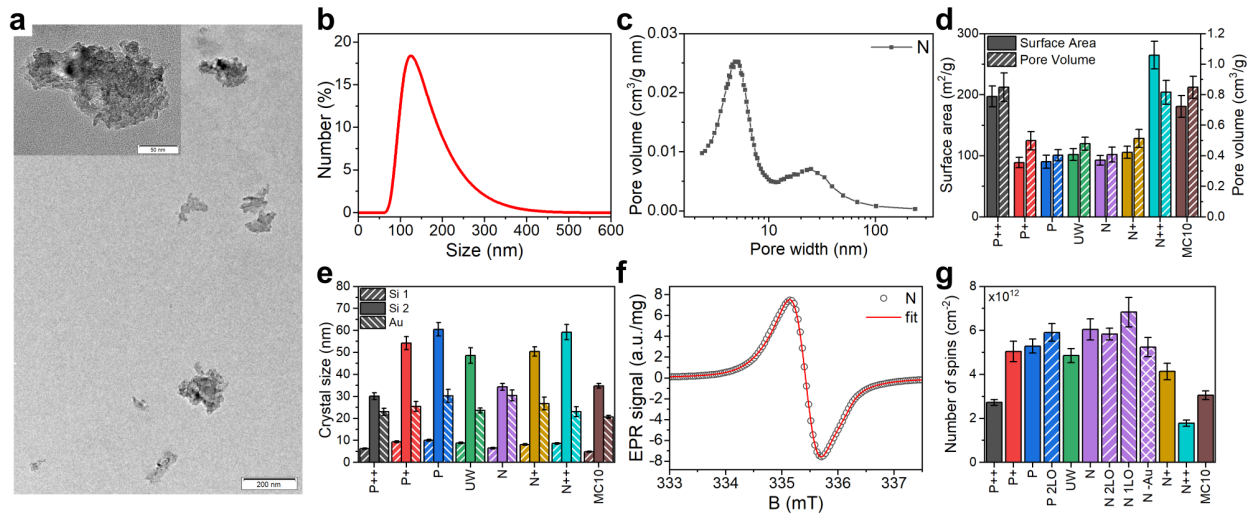


Figure 1: Characterization of PSi NPs. (a) Typical transmission electron microscopy image of PSi NPs dried out of suspension; the inset shows the high magnification view. (b) Hydrodynamic size distribution of the N PSi NPs in water suspension. (c) Pore size distribution of N Si powder after LL-MACE. (d) Specific surface areas and pore volumes obtained from N₂ sorption measurements of Si powders after LL-MACE. (e) Crystalline sizes of pore walls in PSi NPs and sizes of Au NPs calculated from X-ray powder diffraction spectra. (f) Electron paramagnetic resonance spectrum of N PSi NPs. The experimental data (black circles) was fitted (red lines) using isotropic P_b^{iso} defect. (g) Number of spins (P_b defects) in Si/SiO₂ interface of PSi NPs formed by thermal oxidation (no label), thermal and two-step liquid-phase oxidation (2LO label), thermal and one-step liquid-phase oxidation (1LO label), and oxidation induced by Au dissolving solution (-Au label).

NPs. Au NPs' size was similar or smaller than etch track pores presumably due to additional pore wall etching by the same mechanism as torturous pore formation and/or general slight degradation in HF solution.

Electron paramagnetic resonance (EPR) spectra (Fig. 1f, Discussion of P_b centers below and Sec. ??, Suppl. Inf.) showed the presence of two typical paramagnetic centers found on oxidized (porous) Si surfaces. The first one is the trigonal $P_b^{(111)}$ center with axial symmetry similar to the ones found on the oxidized planar (111) and porous Si surfaces ($g_{\parallel} = 2.00185$ $g_{\perp} = 2.0081$).^{25,43,44} The second center is the isotropic P_b^{iso} commonly observed in oxidized porous Si ($g = 2.0055$).^{43,45-49} EasySpin⁵⁰ was used to simulate the experimental EPR spectra to obtain the relative weights of the $P_b^{(111)}$ and P_b^{iso} centers in our samples (Sec. ??, Suppl. Inf.). The simulations gave the typical weights of 10 – 20% for the $P_b^{(111)}$ and 80 – 90% for the P_b^{iso} . It was expected that P_b^{iso} is the dominant center due to the random nature of pore formation in LL-MACE and thermal oxidation in air. Hyperfine (HF) interaction with the central ²⁹Si was also observed (Sec. ??, Suppl. Inf.) and measured to be in the range of $A = 325 - 431$ MHz, which coincided well with $A_{\parallel} = 210$ MHz and $A_{\perp} = 417$ MHz for the planar $P_b^{(111)}$ center.⁴⁴ The number of all types of P_b centers per unit area and per mass varied between $(1.8 - 6.8) \cdot 10^{12} \text{ cm}^{-2}$ (Fig. 1g) and $(4.4 - 6.3) \cdot 10^{15} \text{ mg}^{-1}$, respectively (Sec. ??, Suppl. Inf.). These values corresponded to the fraction of total P_b centers per silicon interface atoms of $f \equiv [P_b]/N_a = 0.23 - 0.87\%$ (where $N_a = 7.83 \cdot 10^{14} \text{ cm}^{-2}$ is the density of lattice sites in the (111) plane). The average distance between the P_b centers was calculated from the concentration per unit area using the nearest neighbors distribution³⁸ derived for the 2D case. The average distances varied between 5.6 nm (P++ and N++ PSi NPs) and 3.0 nm (N PSi NPs). Correspondingly, the dipolar interaction between the electron spins of P_b centers varied from about 2 MHz to 12 MHz for the same samples, respectively. The estimated dipolar interaction strength rather well coincided with the P_b^{iso} Lorentzian linewidth of 0.43 ± 0.60 mT.

We performed DNP NMR polarization and relaxation studies at four different conditions

(Tbl. 2). The two conditions of 3.34 T (3.4 K) and 6.7 T (1.4 K) were applied to all of the samples, while using the two other conditions only few selected samples were measured. In most of the cases, frequency modulation was used. At 3.35 T (1.5 K) we verified that frequency modulation enhanced the DNP process in line with the previous results.^{9,26}

Table 2: Summary of the DNP conditions.

B_0 , T	T , K	W^a , mW	$\Delta\nu_{\text{FM}}^b$, MHz	ν_{FM}^c , kHz
3.34	3.4	200	~ 150	1
3.35	1.5	80	100	1
6.7	1.4	30	200	3
7	3.4	200 ^d	300	10

^a Microwave power; ^b Frequency modulation bandwidth; ^c Frequency of the modulation; ^d Silver-plating the waveguide approximately doubled the MW power reaching the sample⁵¹ for the nominal 200 mW output of the source

The measured DNP profiles followed the symmetry of the EPR spectrum with the positive and negative DNP lobes located at a similar distance to the central zero crossing of the DNP enhancement (Sec. ??, Suppl. Inf.). The zero crossing of the DNP enhancement coincided with the center of the EPR line in agreement with previous works with endogenous defects in Si.^{26,30}

²⁹Si polarization buildup data at 6.7 T (1.4 K) for the thermally oxidized PSi NPs with various dopants are depicted in Fig. 2. The data was corrected for the effects of RF pulses using the iterative correction algorithm and fitted using the one-compartment model.⁵² We confirmed that the algorithm correctly recovered the genuine buildup dynamics from high sampling rate data in Fig. 2 using a low sampling rate of 30 min for the P sample (Fig. ??, Suppl. Inf.). The one-compartment model assumes a monoexponential buildup and decay dynamics as observed in all our samples and employed experimental conditions (Sec. ??, Suppl. Inf.). The model is applicable to most of the previously studied Si NPs and nanodiamonds^{10,14,26,28,34} whereas micrometer-sized Si particles and diamonds typically require

biexponential fitting.^{8,26,28,53,54}

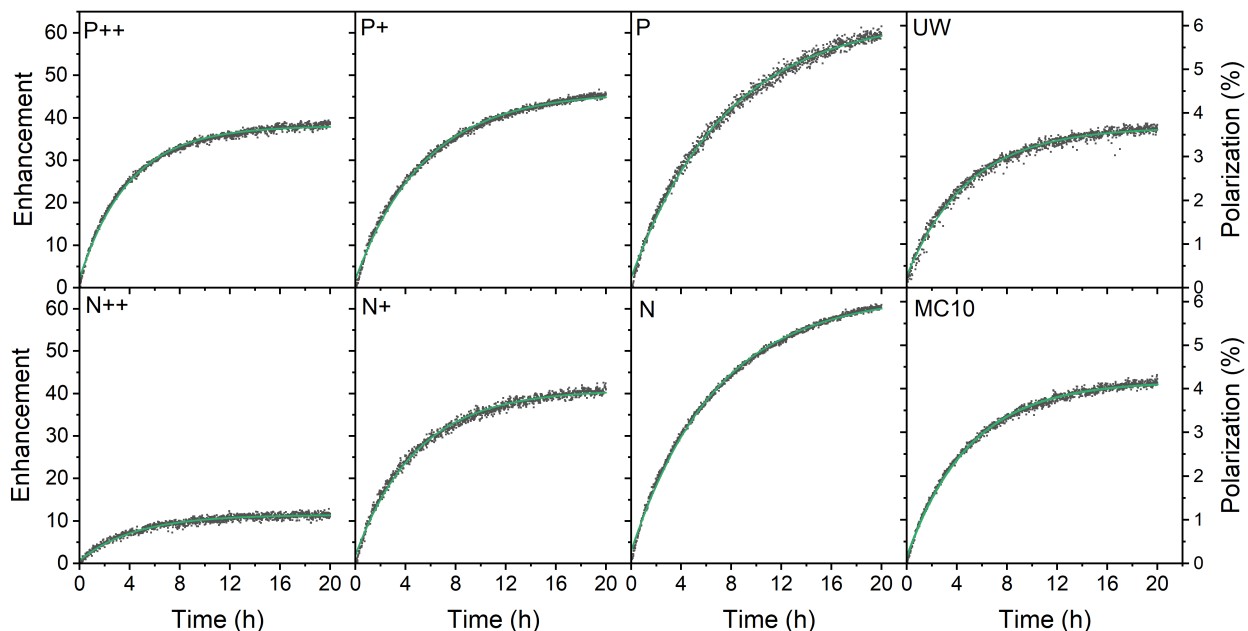


Figure 2: Dynamic nuclear polarization of thermally oxidized PSi NPs with different dopants after correcting for perturbation by the RF pulses⁵² (dark squares) and single exponential fit (green lines) at 6.7 T and 1.4 K. The microwave frequency was set to 187.82 GHz with a 150 MHz bandwidth, 3 kHz modulation, microwave power is 30 mW. The enhancement is relative to the thermal polarization of ^{29}Si nuclear at the polarization buildup conditions. For a characterization of the various samples, see Table 1.

The polarization buildup (at 6.7 T and 1.4 K) was highly dependent on the doping degree. The lowest polarization was found for the highly doped P++ and N++ samples but with significant difference between them despite the similar doping level of the starting Si powder (Tbl. 1). Since none of the doping atoms contributes to DNP directly but could increase the paramagnetic relaxation, the assumption could be made that the best sample would be the one with the least number of dopants *i.e.*, intrinsic Si (UW in Fig. 2 and Table 1). This is, however, not what we found experimentally; the highest polarization levels were obtained for lightly doped P and N samples. Moreover, the relatively impure polycrystalline MC10 PSi NPs showed slightly better DNP polarization and similar buildup times than moderately doped P+ and N+ samples. Such polycrystalline grades could thus be a cheaper alternative to electronics grade sample with sufficiently good DNP properties.

The DNP characteristics changed significantly at 3.34 T and 3.4 K (Fig. 3a and ??, Suppl. Inf.). The polarization buildup times (Fig. 3b) for all samples almost halved compared to 6.7 T (1.4K). The observed relative enhancements were significantly higher at 3.34 T especially for the low B doped PSi NPs compared to the 6.7 T data. The *n*-type samples demonstrated only moderate enhancement increases with the N sample showing even lower enhancement than at 6.7 T. However, the estimated absolute ^{29}Si polarization level was still higher at 6.7 T compared to 3.34 T (Figures 2 and ??, Suppl. Inf.) as enhancements are calculated relative to the ^{29}Si Boltzmann equilibrium polarization at the corresponding magnetic-field strength and temperature.

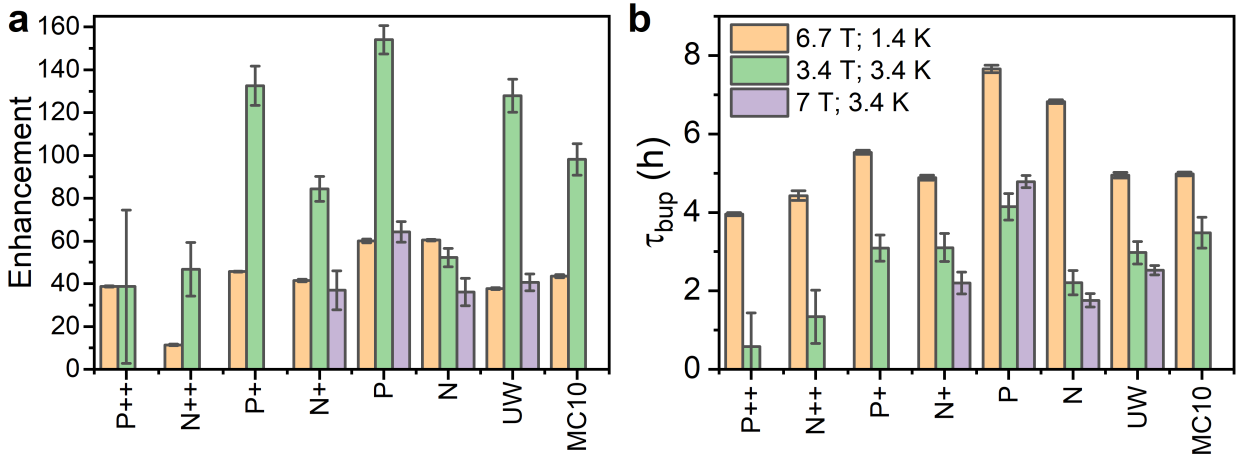


Figure 3: Comparison of ^{29}Si nuclear polarization enhancement (a) and polarization buildup time (b) for PSi NPs at 6.7 T (1.4 K) (orange bars) as well as 3.34 T (3.4 K) (green bars) and 7 T (3.4 K) (violet bars). The enhancement and buildup time are corrected for perturbations by the RF pulses.⁵² MW frequency modulation was employed in all the experiments with the modulation bandwidth and modulation frequency of 300 MHz and 1 kHz at 6.7 T; 300 MHz, 1 kHz at 3.34 and 7 T, respectively. MW powers were 30 mW at 6.7 T and 200 mW at 3.34 and 7 T.

In order to clarify the influence of the experimental conditions on DNP, we performed selected measurements at 7 T (3.4 K) to discriminate between field and temperature dependent changes (Fig. 3 and ??, Suppl. Inf.). The decreased polarization for the N PSi NPs clearly followed the same trend as at 3.34 T while the absolute enhancement values and buildup times for P and UW samples were close to the 6.7 T data. The similarities for P

and UW samples were even more striking provided the MW power was 30 mW at 6.7 T compared to 200 mW at 7 T. We then verified at 7 T (3.4 K) that 200 mW and 20 mW provided similar enhancements at 7 T making the comparison between 6.7 T and 7 T possible despite the large difference in MW power (Fig. ??, Suppl. Inf.). We, therefore, conclude that temperature plays the crucial role in DNP performance of *n*-type PSi NPs, while it has less influence on the *p*-type samples. The temperature dependence for *p*-type samples was further investigated at 3.35 T (1.5 K) (Fig. ??, Suppl. Inf.). We found a significant decrease of enhancement levels compared to the other conditions with minor differences between P and P++ PSi NPs. In the discussion section the differences between the samples at different temperatures and magnetic field are related to the electron spin-lattice relaxation and inhomogeneously broadened EPR line shape, respectively.

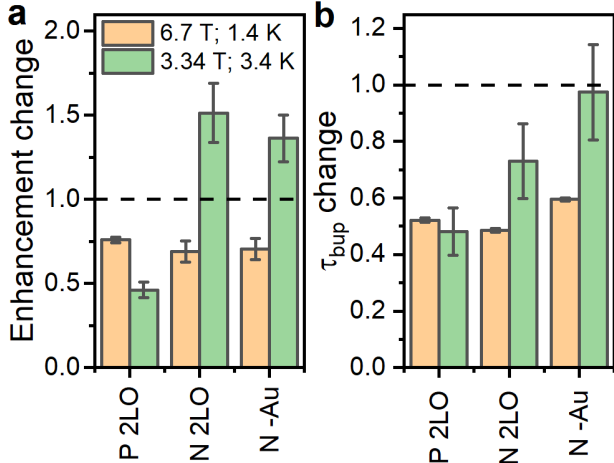


Figure 4: Relative change of the enhancement (a) and polarization build up time (b) due to oxidations for P and N samples. The 2LO oxidation indicates the two-step liquid oxidation (Sec. ??, Suppl. Inf.) performed after the thermal oxidation. For the N -Au, oxidation emerged during the Au removal after LL-MACE (Experimental section). The dashed line indicates no change *i.e.*, the relative change of 1.0. The absolute values are in Fig. ??, Suppl. Inf.

In addition to the thermal oxidation used to create P_b centers on differently doped PSi NPs, we applied liquid oxidation³⁹ to the P and N PSi NPs. Liquid oxidation reduced the number of surface hydrogen in $-\text{Si}_y\text{H}_x-\text{Si}-\text{H}$ and $-\text{O}_3\text{SiH}$ surface groups (Section ??, Suppl. Inf.), which is an important step towards an improved surface coating for biomedical appli-

cations.⁴⁰ Changes in the PSi NPs oxide caused by liquid oxidation affected the the p - and n -type Si samples differently. The same is true for the measurements with different DNP conditions (Fig. 4 and Figs. ??, ??, ??, Suppl. Inf.). For the P sample, enhancement dropped significantly both for the 6.7 T (1.4 K) and 3.34 T (3.4 K), with the higher drop for the latter DNP condition. Contrary to the P sample, liquid oxidation of the N sample increased the enhancement about 1.5 times at 3.34 T (3.4 K), while at 6.7 T (1.4 K) the enhancement decreased. The similar trend for different DNP conditions was observed for the N -Au sample, which was oxidized in the Au dissolution medium. The polarization build up times were affected in a more consistent manner (Fig. 4b). For all the samples and oxidations, the buildup times shortend to 0.5 – 0.7 times the buildup time of the thermally oxidized N or P PSi NPs. Clearly, there is a further room to explore the influence of oxidation, doping, and DNP conditions on the DNP via P_b centers than is reported herein.

Finally, we verified that the presence of Au NPs left in PSi NPs after LL-MACE had little impact on DNP performance. For verification, we applied an iodine-based Au etchant to the N PSi NPs directly after LL-MACE (no thermal oxidation). The Au dissolution resulted in decrease of Au content from 0.37% for N PSi NPs to 0.02% for N-Au PSi NPs as measured by XRF. Since the Au etchant is a strong oxidative solution, the dissolution process also oxidized the PSi NP surfaces which are hydrogen terminated and hydrophobic after LL-MACE. Indeed, the outcome of the etchant-induced oxidation was relatively similar to the effect of the liquid oxidation at least on the N PSi NPs (Fig. 4b).

Table 3: Relaxation time of the selected PSi NPs at 7 T and room temperature after DNP at 3.34 T and 3.4 K.

Abbreviation	τ_{dec} , min
P	75 ± 3
UW	67 ± 8
N	52 ± 5

After collecting the DNP data for the various samples at 3.34 T and 6.7 T, we selected the P, UW and N samples for the room temperature relaxation measurements (Fig. ??,

Suppl. Inf.). For this, the samples were hyperpolarized at 3.34 T (3.4 K) for around 20 h and subsequently transferred to the nearby temperature-controlled (300 K) 7 T setup. At room temperature, the differences between the τ_{dec} of the selected samples diminished compared to the low temperature results (Table ??, Suppl. Inf.). Nevertheless, a smaller τ_{dec} for the N sample compared to the P and UW samples was observed. The P and UW PSi NPs demonstrated the longest depolarization times among the Si NPs so far proposed for MRI with a detectable NMR signal after more than 4 hours of room temperature relaxation.

Discussion

P_b centers

P_b centers have been widely investigated by EPR both on atomically flat specific crystalline planes and in porous Si because of their importance in metal-oxide-semiconductor devices^{23,45} and to elucidate their influence on photoluminescent properties of porous Si.^{46,47,55,56} Different types of P_b centers have been identified with some ambiguity in their naming. Following Brower,²⁵ a P_b center is a localized dangling bond of a Si atom backbonded to three Si atoms at the Si/SiO₂ interface on the (111) crystalline plane (Si₃ ≡ Si·). We denote this center as $P_b^{(111)}$ for clarity. P_{b0} and P_{b1} centers are two distinct centers on the oxidized (100) plane with axial and rhombic symmetries,⁵⁷ respectively. Due to structural similarity of $P_b^{(111)}$ and P_{b0} centers, quite commonly these centers are interchangeably denoted as P_b or P_{b0} in the published literature *e.g.*, in refs.^{44,45}

The trigonal symmetry of $P_b^{(111)}$ centers dictates the trigonal symmetry of the g -factor and HF tensor resulting in $g_{\parallel} = 2.00185$, $A_{\parallel} = 230 \pm 25$ MHz and $g_{\perp} = 2.0081$, $A_{\perp} = 420 \pm 15$ MHz as determined by angular resolved EPR.⁴⁴ The lineshape has been found to vary depending on the mutual orientation of [111] crystalline direction and the external magnetic field. It has Lorentzian shape with peak-to-peak linewidth $\Delta B_{pp}^L = 0.22 \pm 0.015$ mT for $\mathbf{B} \parallel [111]$ and Gaussian shape with $\Delta B_{pp}^G = 0.82 \pm 0.05$ mT for $\mathbf{B} \perp [111]$ indicating the presence of

g_{\perp} strain with $\Delta g \approx 0.0045$. Hyperfine interaction with the nearest (backbonded) neighbor ^{29}Si nuclei has also been resolved with a HF constant $A_{\text{nn}} = 41.5 \pm 0.5$ MHz. Note, that in the literature A_{nn} is denoted as superhyperfine interaction in some cases.⁵⁸

The analysis of the HF tensor in terms of one-electron molecular orbitals²⁵ gave the 12% s -like and 88% p -like wave function character with the total spin-density of about 80% localized on the central $\text{Si}\cdot$ atom. The spin density distribution together with the large HF interaction energies indicate the Fermi-contact interaction to be the dominant one between the P_b electron and the central and neighbor ^{29}Si nuclei. The corresponding dipolar HF splitting is up to ~ 65 MHz and ~ 1.5 MHz for the central and the nearest-neighbor nuclei, respectively. Further from the nearest neighbors, the HF interaction is supposed to be governed by the dipolar part, which drops rapidly with distance. The estimated dipolar part gives the coupling strength of ~ 10 kHz for a ^{29}Si at a distance of two lattice constants.

In oxidized porous Si films, X-band EPR (9 GHz) performed at room temperature^{43,45-49} and in the range of 4–20 K temperature^{8,59,60} has demonstrated two general classes of P_b centers depending on the oxidation conditions. The first class has been observed in both (100)- and (111) crystallographic planes of porous Si oxidized under the controlled oxygen, hydrogen and moisture content. It is reminiscent of $P_b^{(111)}$, P_{b0} , P_{b1} centers found on the corresponding oxidized crystalline planes.^{23,25,44,45,61-63} Among these, the dominant center is $P_b^{(111)}$ due to the simultaneous presence of four possible interfaces (111), ($1\bar{1}1$), ($1\bar{1}\bar{1}$), ($\bar{1}\bar{1}1$).⁴³ This center exhibits similar axial symmetry, g -factors and HF constants, s and p spin densities as the $P_b^{(111)}$ center on the corresponding crystalline plane.^{43,48} Highlighted difficulties to detect (100) P_{b0} and P_{b1} centers^{43,64,65} have been attributed to the dominance of $P_b^{(111)}$ center and to the reconstruction of (100) P_{b0} centers in porous Si⁴⁷ (reconstruction is not efficient on a planar (100) Si surface⁴⁶). Therefore, the measured EPR spectra in controllably oxidized porous Si closely follows the features of crystalline Si samples including angular dependence of g -factors and linewidths.⁴³ Furthermore, EPR spectra from oxidized porous Si are comparable with the ones obtained at K- (24 GHz) and Q-band (35 GHz) at room and

1.4 – 20 K temperatures^{25,44,61,62} on the planar Si surfaces provided that spectra were taken under non-saturating condition. These conditions required low microwave powers at liquid He temperatures due to strong saturability and long T_{1e} time up to approximately 80 ms.⁶⁶

The second class of P_b centers in porous Si develops under uncontrolled native⁴⁶ or thermal oxidation in air,^{49,55,60} and during thermal annealing.^{48,49,56} This P_b^{iso} center is characterized by isotropic $g = 2.0055$, its peak-to-peak linewidth is $\Delta B_{pp} \approx 0.6 - 0.8$ mT with contributions from homogeneous and inhomogeneous broadening.^{46,59} Although the g -factor is isotropic, the linewidth retains anisotropy which follows the trigonal structure similar to the $P_b^{(111)}$ with the smallest linewidth value for $B \parallel [100]$ (0.6 mT) and the largest value $B \parallel [111]$ (1.2 mT). Thus, compared to P_b^{iso} , the P_b centers formed on a corresponding Si plane, have much narrower linewidths. Electron spin relaxation times of P_b^{iso} have received less attention and, therefore, are compared to commercial samples previously investigated for DNP,²⁶ although they might have substantial amount of paramagnetic amorphous Si centers.²² Nevertheless, the measured T_{1e}^{slow} and T_{2e} show rather similar values to $P_b^{(111)}$ equal to 10 – 70 ms and 0.1 – 2 μs at 10 K, respectively.

According to the EasySpin⁵⁰ fitting (Section ??, Suppl. Inf.), P_b centers in the oxidized LL-MACE samples were represented by high number of P_b^{iso} and few $P_b^{(111)}$ centers with their total surface densities in the range of $(1.8 - 6.8) \cdot 10^{12} \text{ cm}^{-2}$ (Fig. 1g) leading to a 3.8 – 7.5 nm average distance between them. The observed line broadening indicated the presence of g -strain typical to the planar $P_b^{(111)}$ centers⁴⁴ ($\Delta g \approx 0.0047$). This strain contributed to the Gaussian peak-to-peak linewidth $\Delta B_{pp}^G \approx 0.8$ mT similar to the planar $P_b^{(111)}$ strain. The Lorentzian part for the $P_b^{(111)}$ was similar to the one obtained by Stesmans and Gorp^{61,62} ($\Delta B_{pp}^L \approx 0.16$ mT, Table ??, Suppl. Inf.), indicating the presence of the dipolar coupling between P_b centers. Liquid oxidation weakly affected the fitting parameters obtained from EasySpin; only the case of N -Au sample stands out with about twice higher g -strain values compared to other samples.

P_b^{iso} centers were fitted with a phenomenological Voigtian lineshape, which gave $\Delta B_{pp}^G =$

0.12 – 0.22 mT and $\Delta B_{pp}^L = 0.45 - 0.50$ mT. The smaller ΔB_{pp}^G was possibly due to less strain for the P_b^{iso} than for the P_b , while the high value ΔB_{pp}^L could indicate stronger dipolar coupling compared to planar (111) P_b centers. $\Delta B_{pp}^L(P_b^{\text{iso}})$ corresponds to $T_2(P_b^{\text{iso}}) \approx 80$ ns. It is possible that the large ΔB_{pp}^L for the P_b^{iso} may indicate the clustering of the P_b centers with orders of magnitude faster electron spin-lattice relaxation rate than for the standalone centers. The investigation of clusters requires further (pulsed) EPR studies to detect the spin-lattice relaxation.

HF interaction with the central ^{29}Si atom was also clearly identified in our X-band EPR measurements (Fig. ??, Suppl. Inf.). The HF constants were in the range of 11.6–15.4 mT or 325–431 MHz and correspond to the typical values of the (111) P_b center with $A_{\parallel} = 210$ MHz and $A_{\perp} = 417$ MHz.⁴⁴ HF coupling with the nearest neighbor (backbonded) ^{29}Si nuclei was not observed due to the large broadening of P_b^{iso} but could be assumed to be present with $A_{\text{nn}} \approx 42$ MHz.²⁵ However, it could be possible that the HF interaction with backbonded ^{29}Si is diminished in our samples due to the backbond oxidation³⁹ of the central ^{28}Si atom. In the case of backbond oxidation, HF interaction with a distant ^{29}Si nuclei can be assumed to be of a purely dipolar nature and scale as r^{-3} with the distance r from a P_b center.

The average distance between the P_b centers assuming their uniform distribution is $d_{\text{ee}} = (3.0 - 5.6)$ nm deduced from their amount per surface area. This distance gives the estimated dipolar coupling D_{ee} on the order of $D_{\text{ee}} = 0.3 - 1.9$ MHz, which is about an order of magnitude lower than the homogeneous line broadening Δ_h calculated from the ΔB_{pp}^L for the P_b^{iso} centers (Tbl. ??, Suppl. Inf.). Such a discrepancy between D_{ee} and ΔB_{pp}^L may indicate clustering of the P_b centers on the ridges and edges of the irregular pore walls and pore openings. For the $P_b^{(111)}$ centers, $\Delta B_{pp}^L \approx (0.001 - 0.004)$ mT, which is more than two orders of magnitude smaller than ΔB_{pp}^L for the P_b^{iso} centers. Combining the need of flat (111) surface and low number of $P_b^{(111)}$ centers, such a small ΔB_{pp}^L possibly indicates a relative isolation of the $P_b^{(111)}$ centers from the others possibly grouped on the ridges.

Summarizing the EPR data towards a DNP mechanism discussion, we highlight the

following main points. The estimated D_{ee} values are strong enough to induce mutual electron spin flip-flops within the EPR line.⁶⁷ The EPR line simulated at the DNP conditions (Fig. ??, Suppl. Inf.) consists of three manifolds: the central strong manifold of total $\sim 95.3\%$ intensity corresponds to the P_b centers with the ^{28}Si central nuclei. The two other manifolds correspond to $m_I = \pm 1/2$ ^{29}Si hyperfine split doublet shifted by $\pm A_{\text{ave}}/2 = \pm(A_{\perp} + A_{\parallel})/4 \approx \pm 162$ MHz and are the replicas of the central line with total intensity of $\sim 4.7\%$. The full width at half maximum (FWHM) of each manifold is ~ 25 MHz at 6.7 T which is about thirty times larger than the D_{ee} , and the total EPR linewidth is more than two orders of magnitude larger than the D_{ee} . Taken together, the anisotropic line broadening provided by the hyperfine interaction and the g factor strain is larger than the nuclear Larmor frequency ω_{on} (between 28 and 60 MHz). Finally, when the central atom of the P_b center is a ^{29}Si , the HF coupling is hundreds of MHz ($A_{\parallel} = 210$ MHz; $A_{\perp} = 417$ MHz). If the nearest neighbor (backbonded) atom is a ^{29}Si nuclei, the HF coupling $A_{\text{nn}} \approx 42$ MHz²⁵ which is much larger than HF coupling in typical biradicals for DNP.⁶⁸

The summarized EPR data satisfies the three main conditions for the triple spin (2 electron spins and 1 nuclear spin) family of DNP mechanisms. Firstly, the dipolar interaction is strong enough within the EPR line. The electron spin flip-flops are then able to either transfer electron Zeeman energy or mutual electron interaction energy to nuclear spin. Second, the EPR line is broader than the nuclear Larmor frequency at all the experimental conditions. Thirdly, part of the electron spins in P_b centers possess HF coupling with ^{29}Si nuclei. Following the ongoing theoretical efforts to understand the triple spin flip DNP,^{67,69-74} we restrain ourselves from going into the specific variants, such as cross effect or thermal mixing DNP. We only highlight that D_{ee} values in our samples support cross effect DNP according to the recent quantum mechanical simulation.⁶⁷ Finally, we also note the results from previous study of nominally undoped Si microparticles, in which the decay of nuclear hyperpolarization was explained through triple spin flips,⁷⁵ emphasizing the importance of triple spin flips in the Si/SiO₂ interface.

Rate limiting step for the DNP buildup

The EPR spectrum extrapolated to the DNP field strength of 3.34 T or 6.7 T consists of three lines (Fig. 5): the central line for P_b at ^{28}Si nuclei is surrounded by the two HF-split lines for $m_I = \pm 1/2$ whose shape is the same as of the central line. Each of the three EPR lines is the combination of the $P_b^{(111)}$ powder average and P_b^{iso} centers. Strain in the Si/SiO₂ interface creates the g -factor anisotropy up to $\Delta g \approx 0.0065$ and introduces significant inhomogeneous line broadening up to ≈ 60 MHz at 6.7 T.

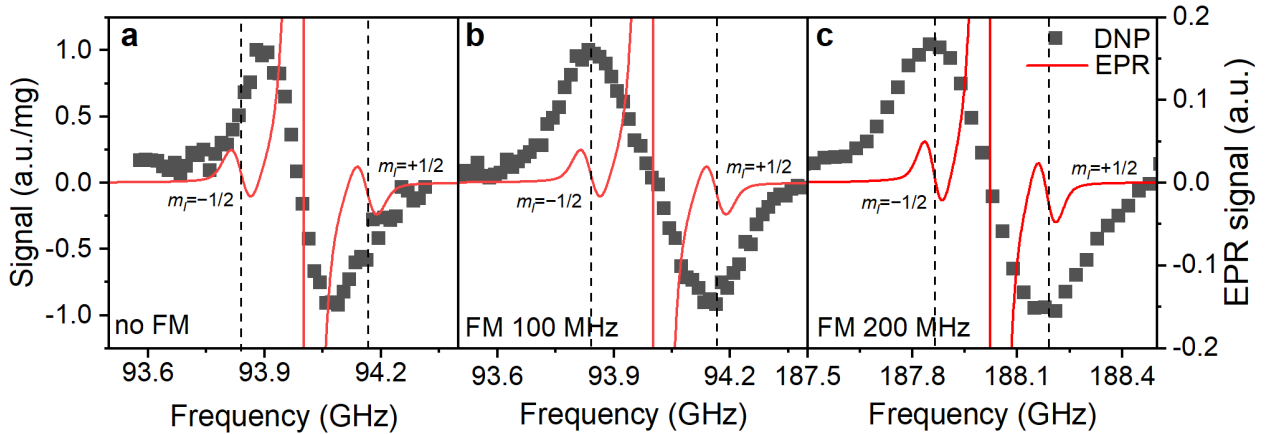


Figure 5: Overlay of the simulated ESR and experimental DNP spectra for the P sample at (a) 3.35 T, 1.5 K without MW modulation (frequency modulation - FM), (b) 3.35 T, 1.4 K with 100 MHz MW modulation and (c) 6.7 T, 1.4 K with 200 MHz MW modulation. ESR spectrum is the frequency-swept spectrum simulated using the model obtained from the experimental data fitting (Fig. 1f, Section ??, Suppl. Inf.).

The DNP profiles show two DNP peaks of positive and negative enhancements with nearly equal amplitude and width (Fig. 5 and ??, Suppl. Inf.). If MW modulation is applied, the maximum and minimum of DNP enhancement in our samples coincides with the frequencies of the HF-split $m_I = \pm 1/2$ doublet in the EPR spectrum (Fig. 5). In contrast, without MW modulation takes a similar featureless shape but frequency difference between the two DNP lobes is narrower although still much larger than the nuclear Larmor frequency ($\omega_{0n}(3.34 \text{ T}) \approx 28 \text{ MHz}$).

In DNP, the strength of HF interaction between electron and nuclear spins determines the

polarization transfer rate constant, which is proportional to the square of the HF coupling A^2 following a perturbation treatment.¹² Owing to the large HF constant ($A_{\parallel} = 210$ MHz; $A_{\perp} = 417$ MHz) between the P_b electron and the central ^{29}Si nuclei, the DNP of these nuclei should be efficient and fast. Even in the unmodulated case, DNP proceeding through the HF interaction with the nearest neighbors (if occupied by a ^{29}Si nucleus) from the ^{28}Si EPR manifold with $A_{\text{nn}} \approx 42$ MHz²⁵ is expected to be fast. MW modulation further improves the DNP and shifts the positive and negative enhancements apart when applied^{9,26,76} as observed in Fig. 5a,b. Interestingly, we found the optimal MW modulation bandwidth to be 100 MHz and 200 MHz at 3.35 T and 6.7 T, respectively. These bandwidths make the maximum positive and negative DNP enhancements to coincide with the $m_I = \pm 1/2$ EPR manifolds. We interpret this coincidence as the indication that the electron-nuclear polarization transfer pathway occurs preferentially through P_b centers with ^{29}Si central nuclei and not through the backbonded nearest neighbor ^{29}Si . The increased transfer efficiency to the central ^{29}Si can be understood by the up to ten times larger HF coupling compared to other possible locations of ^{29}Si , since the polarization transfer rate scales approximately with the HF coupling squared.

Independent of the exact location of ^{29}Si nucleus involved in the initial HF-mediated polarization transfer, the polarization needs to penetrate from the surface nuclei into the pore wall cores of the PSi NPs for which we invoke the concept of nuclear spin diffusion (nSD).^{12,77} The dipolar interaction between nuclei induces nuclear spin flip-flops — a zero-quantum (ZQ) process with no net change of the total magnetic quantum number. This ZQ process can cause an effective spatial transport of magnetization that can be described by a diffusion equation if a nuclear polarization gradient is present in the sample.

The nSD constant in Si was previously approximated to be $D_{\text{diff}} \approx a^2/30T_{2\text{n}}$,¹³ where a is the average distance between ^{29}Si nuclei in a cubic lattice and $T_{2\text{n}}$ is the nuclear spin-spin relaxation time. In the approximation of D_{diff} , it was implicitly assumed that the experimentally measured single quantum (SQ) $T_{2\text{n}} = T_{2\text{n}}^{\text{SQ}}$ is identical to the ZQ $T_{2\text{n}}^{\text{ZQ}}$ process involved in

nSD. For now, we use the bulk Si $T_{2n} \approx 80-100 \text{ Hz}^{13}$ which results in $D_{\text{diff}} \approx 0.5-1.7 \text{ nm}^2\text{s}^{-1}$, consistent with the approximate value of $0.6 \text{ nm}^2\text{s}^{-1}$ in Si microparticles estimated by Dementyev *et al.*⁵³ Therefore, for the polarization to diffuse from the surface into the pore wall's cores $r_{\text{wall}}/2$, a time scale of only $\sim 8 \text{ s}$ or $\sim 140 \text{ s}$ ($\tau_{\text{diff}} = \langle (r_{\text{wall}}/2)^2 \rangle / 6D_{\text{diff}}$) is required for the tortuous or etch track pores, respectively (Fig. 1c,e).

Taken together, both the polarization of the central P_b ^{29}Si and the nuclear spin diffusion throughout pore walls are relatively fast processes compared to the measured buildup and decay times at all the DNP conditions (Fig. 2 and Sec. ??, Suppl. Inf.). In order to explain the long polarization buildup and decays we shall recall that there are ^{29}Si nuclei with remarkably strong HF interaction — the central and backbonded P_b nuclei. Between these strongly HF-coupled ^{29}Si spins and the bulk spins exists a large shift in frequency/energy, which is further enhanced due to sparsity of ^{29}Si in the naturally abundant PSi NPs. Such frequency shifts suppress nuclear flip-flop transitions and create a so called 'spin diffusion barrier'.^{12,77} The transfer from the HF-shifted nuclear spins to the bulk is, therefore, restrained, making it the rate limiting step in the DNP buildup.

For the nuclear polarization to diffuse across the large HF-induced frequency gradient ('spin diffusion barrier'), the electrons need to modify the effective nuclear-nuclear spin interactions.⁷⁸⁻⁸¹ A high abundance of nuclear spins close to the electron wave function localization then becomes essential for a fast buildup with high enhancement⁶⁸ as it limits the frequency differences between spin pairs required for spin diffusion into the bulk and increases the nuclear dipolar couplings.

Another possible explanation for the long buildup time invokes the polarization transfer towards weakly HF-coupled spins. In this case distant ^{29}Si nuclei are polarized directly by the dipolar coupling to a P_b electron spin. This process has a low probability since the HF coupling between a P_b electron and a distant ^{29}Si nucleus rapidly vanishes with the distance between them. For a nuclei located at a distance of three lattice constants, the HF interaction is $A_{\text{nndipolar}} \approx 3.5 \text{ kHz}$, yielding low rates of direct polarization transfer.

The direct polarization transfer hypothesis, however, possess few flaws. First, even the $A_{\text{nn}}^{\text{dipolar}} \approx 3.5 \text{ kHz}$ is strong enough to exceed the nuclear dipolar coupling $C^{ij} \approx 400 \text{ Hz}$ for naturally abundant Si breaking the nSD condition of $|A_{\text{nn}}^i - A_{\text{nn}}^j| \leq C^{ij}$ (i, j denote two nearby ^{29}Si nuclei). Second, the direct polarization transfer fails to explain the $m_I = \pm 1/2$ DNP enhancements and zero DNP for the central ESR peak (Fig. 5). Taken together, the small $A_{\text{nn}}^{\text{dipolar}}$ and the EPR-DNP relation makes this process rather inefficient in our samples.

Finally, we highlight that 95.3% of the P_b centers have magnetically inactive ^{28}Si or ^{30}Si central nuclei. Therefore, in addition to the low probability of transfer from the central ^{29}Si to the distanced bulk, only 4.7% of P_b contribute to the hyperpolarization buildup. According to the sample characterization data, a typical PSi NP of 150 nm size, 55% porosity ($0.55 \text{ cm}^3\text{g}^{-1}$ pore volume) and $100 \text{ m}^2\text{g}^{-1}$ surface area contains on average $2.3 \cdot 10^6$ ^{29}Si nuclei and $1.3 \cdot 10^4$ P_b centers (Fig. 1b-g). Therefore, a straightforward but incorrect calculation yields the number of ^{29}Si to be polarized by one P_b center equal to ~ 180 — a common value for partially deuterated water glycerol mixtures (DNP juice).⁸² However, the number of ^{29}Si nuclei that are central to the P_b electrons is only 4.7% of the total number of nuclei. This leads to the ~ 3800 nuclei to be polarized by one P_b center, a much lower value than in typical DNP samples.

Rate limiting step for the polarization decay

The polarization decay in Si particles with endogenous electronic centers has been commonly considered to be limited by nSD from bulk to the centers.^{8,33,75} The arguments of low electron polarization at room temperature and orders of magnitude lower T_{1e} and T_{2e} than at DNP conditions further supported the hypothesis of nSD limiting relaxation. Although these arguments seem to be a reasonable for micrometer-sized Si particles, they are hardly applicable to our case of PSi NPs or to other types of Si NPs.^{26,30,34} If nSD is the rate limiting step for the relaxation in our samples, the polarization decay time τ_{dec} at room temperature should be tens of seconds at the slowest, according to the estimated $D_{\text{diff}} \approx 0.5 - 1.7 \text{ nm}^2\text{s}^{-1}$. Unless

this estimation is orders of magnitude incorrect, which is unlikely, nSD fails to explain the room temperature relaxation times in nanoscale Si.

We, therefore, propose that even at room temperature the nuclear relaxation is governed by the same process as at the DNP conditions *i.e.*, by the electron modified nSD across the 'spin diffusion barrier'. Such an interpretation would be in good agreement with isotope enrichment experiments³⁴ resulting in larger nuclear dipolar couplings. There, the ²⁹Si abundance was varied between 4.7 and 15% which caused a 3-fold decrease in τ_{dec} (from 48 to 17 minutes). Furthermore, naturally abundant Si NPs for 160 nm³⁴ and 50 nm^{9,26} bulk particles as well as the porous particles in this work all give similar room temperature relaxation times of around 50 minutes. Such a similar relaxation time would be consistent with the proposed time limiting step of polarization transfer across the 'spin diffusion barrier'.

The major open question with the proposed rate limiting step of the room temperature decay is the lack of knowledge of the electron relaxation times w.r.t. to the nuclear Larmor frequency ω_{0n} . If the relaxation rate is much smaller than ω_{0n} , the HF couplings are not averaged and the situation is similar to low temperature DNP conditions. For much faster relaxation rates than ω_{0n} , the thermal electron polarization at room temperature and 7 T of 1.6% leads to a significant pseudo-contact shift due to the partially averaged HF couplings. Even in this averaged case the pseudo-contact shift is large compared to the nuclear dipolar couplings mediating the nSD.

The nSD across the barrier may also provide additional insights into the ²⁹Si abundance dependence of polarization decay beyond the D_{diff} change. For example, the increase of ²⁹Si abundance may improve the diffusion across the barrier since the relative pseudo-contact or HF-induced frequency shifts decrease and nuclear dipolar couplings increase when the ²⁹Si nuclei are located closer to the central P_b ²⁹Si spins.⁶⁸ The enhanced transport across the spin diffusion barrier might be supported by isotope labelling experiments in Si NPs.³⁴ There, both the polarization buildup and decay times substantially and nonlinearly decreased with the increase of ²⁹Si density.

Field and temperature dependence of DNP

Fig. 3 compares the enhancements and buildup times of the different samples at 3.34 T (3.4 K), 7 T (3.4 K) and 6.7 T (1.4 K). At 6.7 T and 7 T, the enhancements are nearly identical for all the samples, except for the N PSi NPs (discussed later). At 3.34 T, the enhancements are 2.7 ± 1.1 times higher than at 6.7/7 T (again, the N sample stands out). The decrease of the DNP temperature from 3.4 K (7 T) to 1.4 K (6.7 T) does not improve the enhancements but extends the buildup time (Fig. 3). Contrasting, the increase of B_0 from 3.34 T to 7 T keeping 3.4 K temperature shows minor effects on the buildup time, often within the experimental uncertainty. At 3.34 T, the decrease of temperature from 3.4 K to about 1.5 K leads to detrimental effects on DNP performance (Fig. ??, Suppl. Inf.) — the enhancements hardly reached the value of 20 for the P PSi NPs.

At the end of the DNP process, we aim to obtain the highest possible absolute nuclear polarization for which low temperature brings a significant benefit. While reducing the temperature from 3.4 to 1.4 K at 6.7 T or 7 T only causes a moderate increase in electron polarization (around 10%), such temperature decrease more than doubles the thermal nuclear polarization. Therefore, the nuclear thermal polarization increase translates the enhancements into more than 6% absolute polarization of the N sample at 1.4 K (6.7 T) (Fig. 2) — the highest polarization achieved in our experiments.

Rate-equation model

In this section, we apply a rate equation model⁵² to deepen the explanation of the observed buildup and decay data. The model allows us to trace back the differences between the samples which stem mostly from variations in the relaxation rates and to a lesser degree from the actual HF-mediated polarization transfer ('DNP injection'). Furthermore, the limited benefit of lower temperatures (1.5 instead of 3.4 K) is traced back to a relaxation enhancement by MW irradiation.⁸³ We first quickly summarize the model before applying it to discern the effects of different experimental conditions and then to compare different

samples for 6.7 T (1.4 K).

The presence of the single rate-limiting step in PSi NPs leads to build-up and decay curves that follow a mono-exponential trend. The mono-exponential nature, in turn, enables us to use the one-compartment rate-equation model to analyze the influence of doping and oxidation on the rate constants that describe the DNP buildup and decay.⁵²

The one-compartment model provides an additional layer of interpretation for the measured enhancements, buildup τ_{bup} and decay τ_{dec} time constants. For the buildups, τ_{bup} is considered to be a composite of the two competing processes: the polarization injection rate to the nuclei, k_{W} , and the nuclear relaxation rate, $k_{\text{R}}^{\text{bup}}$. Together with the thermal electron polarization $P_{0\text{e}}$, we can write for the one-compartment buildup model:⁵²

$$\frac{dP_{\text{n}}(t)}{dt} = (P_{0\text{e}} - P_{\text{n}})k_{\text{W}} - k_{\text{R}}^{\text{bup}}P_{\text{n}}, \quad (1\text{a})$$

$$\tau_{\text{bup}}^{-1} = k_{\text{W}} + k_{\text{R}}^{\text{bup}}, \quad (1\text{b})$$

$$P_{1\text{n}} = P_{0\text{e}} \frac{k_{\text{W}}}{k_{\text{W}} + k_{\text{R}}^{\text{bup}}}, \quad (1\text{c})$$

where $P_{1\text{n}}$ is the steady-state nuclear polarization reached by the end of the DNP process.

The rate constants are then calculated from the maximum thermal electron polarization $P_{0\text{e}}$ at the DNP conditions together with the measured τ_{bup} and steady-state DNP polarization $P_{0\text{n}}$ obtained from the mono-exponential fitting. Eqs. 1b,1c can be rewritten to⁵² $k_{\text{W}} = \tau_{\text{bup}}^{-1}P_{1\text{n}}/P_{0\text{e}}$ and $k_{\text{R}}^{\text{bup}} = \tau_{\text{bup}}^{-1}(1 - P_{1\text{n}}/P_{0\text{e}})$. For the decays, the model is much simpler than for the buildups since there is no polarization injection. The decay time and relaxation rate during decay are thus simply related as $k_{\text{R}}^{\text{dec}} = \tau_{\text{dec}}^{-1}$.

In the following, we will use the rate constants to better understand the effects of experimental conditions (field strength, temperature) and sample doping. The two rates k_{W} and $k_{\text{R}}^{\text{bup}}$ calculated from the τ_{bup} and $P_{0\text{n}}$ from Fig. 3 are depicted in Fig. 6a to highlight the influence of the experimental conditions (for all the samples we refer to Sec. ??, Suppl. Inf.). The build-up and decay rate constants for all samples at 6.7 T, 1.4 K are shown in Fig. 6b.

We start applying the one-compartment model by the recap of experimental conditions (Fig. 6a). We find the highest injection rates k_W to be at 3.34 T, 3.4 K except for the N sample, which has the highest k_W at 7 T, 3.4 K. For the P-doped PSi NPs, k_W are similar at 1.4 K and 3.4 K for $B_0 \approx 7$ T despite the much lower MW power of 30 mW applied compared to 3.4 K setups (200 mW at 3.34 T and 400 mW at 7 T). The single experiment with 20 mW microwave power at 7 T (3.4 K) gives similar results compared to full MW power of 200 mW (Fig. ??, Suppl. Inf.). Despite at 3.35 and 1.5 K the enhancements are the lowest, k_W are similar to 3.4 K (3.34 T) owing to the highest buildup relaxation rates observed.

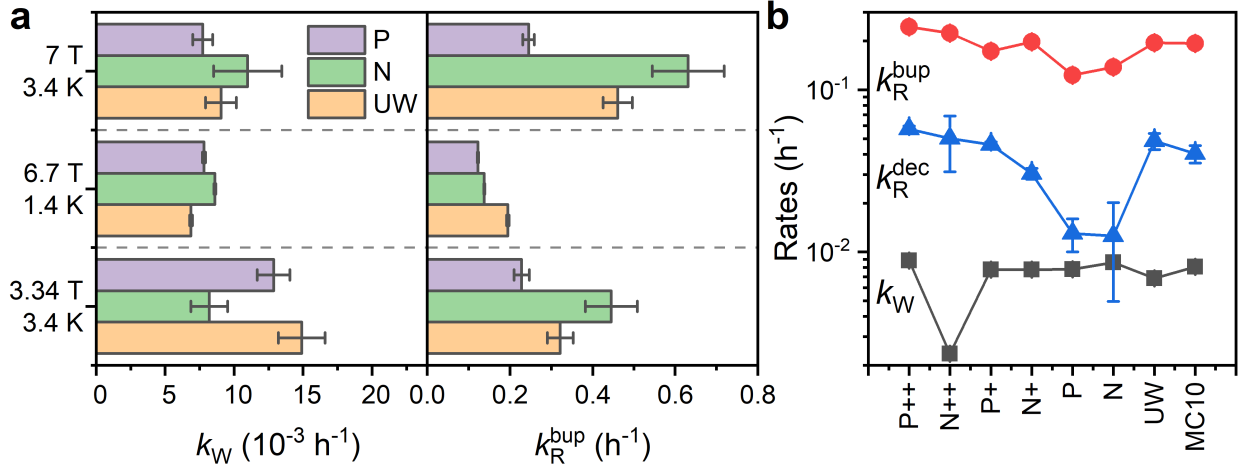


Figure 6: One-compartment model parameters calculated from the monoexponential fitting of the buildup and decays. (a) Comparison of the k_W and k_R^{bup} at the three experimental conditions for the selected P, UW and N PSi NPs. Note the 10^{-3} scale for the k_W . (b) Polarization buildup (dark squares and red circles) and decay (blue triangles) rates for the PSi NPs with different doping and oxidation. The data was acquired at 6.7 T, 1.4 K. Lines are a guide for the eye.

Build-up relaxation rates k_R^{bup} significantly differ between the experimental conditions and strongly affect the achieved enhancements and nuclear polarizations. k_R^{bup} rates are typically several times lower at 1.4 K (6.7 T) than at 3.4 K (Fig. 6a) consistent with the decrease of electron spin lattice relaxation time.²⁴ Contrary to 6.7 T, at 3.35 T and 1.5 K k_R^{bup} is the highest detrimentally affecting nuclear polarization gain (Fig. ??, Suppl. Inf.). At 3.4 K, k_R^{bup} is generally smaller for 3.34 T compared to 7 T despite the higher thermal electron polarization at 7 T (around 90% instead of 60%).

The relaxation rate constants during the decay $k_{\text{R}}^{\text{dec}}$ conformed to the following trend: slowest at 1.4 K (6.7 T) (Fig. 6)b, intermediate at 7 T (3.4 K) and fastest at 3.34 T (3.4 K) (cf. Figs. ??, ?? and Tab. ??). This trend is consistent with the gradual increase of electron spin polarization from $\sim 60\%$ at 3.34 T, 3.4 K up to $\sim 99.7\%$ at 6.7 T, 1.4 K. The similar relaxation reduction at temperatures below ~ 2 K at ~ 7 T has been observed in our setups for ^1H glassy matrices⁸³ as well as for diamonds before (data not shown). These results are attributed to high electron polarization which strongly reduces paramagnetic relaxation approximated by $1 - P_{0\text{e}}^2$.⁸⁴

The discrepancy between relaxation rate constants during buildup ($k_{\text{R}}^{\text{bup}}$) and decay ($k_{\text{R}}^{\text{dec}}$) is the most pronounced at 1.5 K with more than order of magnitude ratio between the two at 3.35 T (Fig. 6b and ??, Suppl. Inf.). At 3.4 K and 7 T the $k_{\text{R}}^{\text{dec}}/k_{\text{R}}^{\text{bup}}$ ratio is in the range of 2.5 ± 0.5 while at 3.34 T the ratio is close to 1 (Sec. ??, Suppl. Inf.). The higher relaxation enhancement by MW irradiation (compared to the decay) at lower temperatures and lower fields is consistent with the results found in Ref.⁸³ which is ascribed to an increased triple-spin flip rate by MW irradiation causing a relaxation enhancement.

Returning to the buildup time τ_{bup} and enhancements (or nuclear polarization $P_{1\text{n}}$) as shown in Fig. 3, experimental conditions of 1.4 K and 6.7 T offer the average k_{W} as well as the lowest $k_{\text{R}}^{\text{bup}}$ and $k_{\text{R}}^{\text{dec}}$ explaining the highest polarization and longest build-up times. The much larger $k_{\text{R}}^{\text{bup}}$ compared to $k_{\text{R}}^{\text{dec}}$ prevents excessively long build-up times but severely hampers achievable polarization levels. The relatively field independent polarization injection rates k_{W} at 3.4 K combined with slightly higher $k_{\text{R}}^{\text{bup}}$ at 7 T than at 3.34 T lead to the similar buildup times and nuclear polarizations with the approximately halved enhancements. The field independent injection rate facilitates further study of this effect since typical DNP models for the electron-nuclear HF-mediated polarization transfer predict the decrease of triple spin flip transition rate with increasing magnetic field strength.^{12,71} Cooling to 1.5 K at 3.35 T results in a very large relaxation rate during the build-up, reflected by a fast build up and low steady-state polarization.

In a last step, we want to have a closer look on the rate equation parameters of the 6.7 T (1.4 K) measurements. For the low steady-state nuclear polarization with respect to the electron thermal polarization ($P_{1n} \ll P_{0e}$), we can simplify Eqs. 1 to

$$\tau_{\text{bup}}^{-1} \stackrel{P_{1n} \ll P_{0e}}{\approx} k_{\text{R}}^{\text{bup}}, \quad (2a)$$

$$P_{1n} = P_{0e} k_{\text{W}} \tau_{\text{bup}} \stackrel{P_{1n} \ll P_{0e}}{\approx} P_{0e} \frac{k_{\text{W}}}{k_{\text{R}}^{\text{bup}}} \quad (2b)$$

such that the information about $k_{\text{R}}^{\text{bup}}$ is mostly encoded on the build-up time and P_{1n} describes k_{W} . The simplification suggests τ_{bup} (together with $k_{\text{R}}^{\text{bup}}$) being rather independent of the overall sample properties (doping, surface area, P_{b} density) but rather depends on the microscopic environment of the different P_{b} centers. Performed correlation analysis supports this observation providing relatively small correlation coefficients below 0.15 in absolute value. The correlation between $k_{\text{R}}^{\text{bup}}$ ($k_{\text{R}}^{\text{bup}}$) and Lorentzian linewidths of both $P_{\text{b}}^{(111)}$ and $P_{\text{b}}^{\text{iso}}$ is on the order of 0.5 – 0.65 evidencing the importance of the interaction between the P_{b} centers. Further studies are required to understand this.

In contrast, k_{W} seems to depend on the density of P_{b} centers (correlation coefficient of 0.57 over all samples). A larger specific surface area results in a lower density of P_{b} center (correlation coefficient of -0.73) suggesting a non-uniform distribution of the P_{b} centers. The surface area (and the pore volume) can be controlled through the doping level (correlation coefficient of 0.90) since it influences the outcome of LL-MACE.^{31,32}

Besides the doping affecting the etching process, high doping would lead to a large number of quenched nuclear spins owing to the extended wave functions of shallow dopants (phosphorous and boron). Furthermore, high doping levels would lead to fast room temperature relaxation.⁷⁵ Cheap polycrystalline grades of relatively high purity can be a good alternative for the electronic grade wafer based PSi NPs although room temperature relaxation times were not measured.

At 6.7 T (1.4 K), the additional liquid oxidation and the oxidation induced by the Au

removal increased the relaxation rates for the P and N samples (Fig. 4). This increase turned into lower enhancements and faster buildup times compared to the thermally oxidized PSi NPs of the same doping density. The influence of additional liquid oxidation remains unclear provided that these oxidations yield little effect on the structure and number of the P_b centers (Fig. 1 and Sec. ??, Suppl. Inf.). In contrast, at 3.34 T (3.4 K), the additional liquid oxidation and oxidation from the gold removal increased the achievable enhancements for N samples without causing a prolonged build-up. We note that the removal of the gold nanoparticle catalyst has little effect on the DNP, suggesting that the nuclear polarization inside the particle is well protected from surface modifications including metallic nanoparticles.

In summary, the differences between the samples is mostly due to different relaxation rates during the build-up. Lower temperatures (1.5 instead of 3.4 K) show at best only a modest improvement in the nuclear polarization owing to more pronounced relaxation enhancement by MW irradiation.⁸³ Combining lower temperatures with higher fields partially suppresses the relaxation enhancement by MW irradiation⁸³ and resulted in the highest nuclear polarizations.

Conclusion

We employed the low-load metal assisted catalytic etching (LL-MACE)^{31,32} method to fabricate a variety of porous Si NPs from electronic grade single crystal Si wafers. This top-down fabrication approach allowed us to vary dopant type and density while achieving nearly identical surface properties and crystallinity in all the NPs. A separate oxidation step led to the formation of electronic P_b centers with similar structure and surface density for all the types of PSi NPs. This resulted in the successful and similar DNP injection in all samples with the polarization differences mostly ascribed to relaxation. The highest steady-state polarizations were achieved with lightly phosphorous or boron-doped samples. Measurements at 7 T (3.4 K) and 3.35 T (1.4 and 3.4 K) gave lower polarization levels than the 6% achieved

at 6.7 T, 1.4 K. Room temperature decay times of the studied samples exceeded one hour — the longest decay time obtained so far in Si NPs to our knowledge.

The gained insights about P_b centers enabled us to shed light on the polarization transfer from the electron spins to ^{29}Si . Our results suggested that the central ^{29}Si nuclei of the P_b centers were first polarized making them essential for the polarization buildup. These nuclei have large hyperfine (HF) shift which presents a barrier for the nuclear spin diffusion (nSD) to spread the polarization into the core of the pore walls. Combined with only 4.7% of the P_b centers having the central ^{29}Si nuclei in the naturally abundant Si indeed results in few hours long polarization buildup constants observed previously in various Si NPs. We, therefore, concluded that the rate limiting step in the DNP of Si NPs via the P_b centers is the polarization transfer across the spin diffusion barrier from the HF shifted central ^{29}Si nuclei to the bulk. Isotope labelling may improve the transport across the spin diffusion barrier and, therefore, improve the NMR signal through the increased enhancement and number of magnetically active spins. The disadvantages of isotope labelling are high sample cost and the decrease of the long room temperature decay time.

We expect that the presented analysis of the sample structure and DNP conditions will provide new pathways to develop versatile MRI imaging agents with acceptable polarization buildups while still keeping the relaxation time on the order of one hour. With the hyperpolarization we envision that virtually any Si-based imaging and/or therapeutic agent can be augmented with the imaging modality without any additional chemical modification.

Experimental

Silicon

Silicon used in this study was electronics grade single crystal (100) Si wafers of different doping (Okmetic Oy, Finland) and polycrystalline 1 – 10 μm Silgrain Supreme MC10 SB powder (Elkem Silicon Products, Norway). The purity of the powder was 99.997% deter-

mined by the supplier, where the main impurities were Fe (14 ppm), Al (6 ppm), Ca (3 ppm), Ti (1 ppm), B (< 1 ppm), and P (< 1 ppm).

Dopant type of the Si wafers was verified by hot point probe method.⁸⁵ Specific resistivity was calculated using a MATLAB (The MathWorks, Inc., USA) script using wafer thickness and resistivity measured with a four-point probe (Jandel Engineering Ltd, UK) connected to a Cropico DO5000 microhmmeter (Seaward Electronics Ltd, UK).⁸⁵ The dopant concentrations were estimated by comparing the measured specific resistivities with the ones calculated using Caughey-Thomas expression³⁶ from electron and hole mobilities at 300 K assuming full ionization of dopant atoms. The average distances between dopant atoms were calculated from the doping densities using the probability density function to find the atom at a distance r .³⁸ Assuming the uniform random distribution of the dopant atoms, the average distance is $\langle r \rangle \approx 0.554 \cdot N_c^{-1/3}$, where N_c is the density of atoms. The equivalent Bohr radii for acceptors were estimated using the expression derived from the hydrogen atom-like model of donor (acceptor): $a_A = \epsilon_r m_0 / m_{eff} \cdot a_0$, where a_0 is the Bohr radius of hydrogen atom, ϵ_r is the relative dielectric permittivity of Si, m_0 is the electron mass, and m_{eff} is the effective mass of a hole. For the donors, more precise value of the electron's effective Bohr radius is given by the geometric mean $a_D = a_{\parallel}^{1/3} a_{\perp}^{2/3} \approx 2.087$ nm, where $a_{\parallel} \approx 1.44$ nm and $a_{\perp} \approx 2.51$ nm are the two radii of the pancake-like wavefunction ansatz for the electron ground state proposed by Kohn and Luttinger.³⁷ The information about Si types and abbreviations used in text are summarized in Table 1.

Porous Si powders

10 – 25 μm powders were prepared by ball-milling Si wafers using Fritsch Pulverisette 7 Premium Line (Fritsch GmbH, Germany). Obtained powders were washed in 3% wt. aqueous H_2O_2 by sonicating them for 1 h in an ultrasound bath.³² Such washing removes possible surface contaminations and ensures reproducibility. The powders were then dried and used to produce porous Si by low-load metal-assisted catalytic etching (LL-MACE) as reported

before.^{31,32} The protocol was scaled up to perform etching of 2 g Si powder batches. Briefly, 2 g of Si powder was first dispersed in 30 ml of acetic acid (Ph. Eur., VWR Chemicals) inside of a 50 ml PTFE dish by 5 min sonication. Then, 30 ml of hydrogen fluoride (HF, 30 – 40%, Merck) was added, and the dish was placed in a water bath on a heat plate under stirring. Next, Au NPs were nucleated on Si powder surfaces using a syringe pump injection of 8.334 ml (= 50 μmol) of 0.006 M Au^{3+} ion solution, which was prepared by dissolving $\text{HAuCl}_4 \cdot 3\text{H}_2\text{O}$ (99.99%, Alfa Aesar, Thermo Fisher GmbH) in water. Injection rate was 333.3 $\mu\text{l}\cdot\text{min}^{-1}$; after it was completed, Si powder suspension was stirred for 5 min more to complete the nucleation of Au^{3+} NPs. The temperature of the water bath was kept at about 39 °C to retain the temperature of the suspension in the range of 51 – 53 °C during etching. The etching was performed by injecting $\text{H}_2\text{O}_2/\text{H}_2\text{O}$ solution using the syringe pump at a rate of 133.3 $\mu\text{l}\cdot\text{min}^{-1}$ (injection time equals to 90 min). The H_2O_2 volume (35 wt.%, Acros Organics, Thermo Fisher GmbH) in the solution was selected to match the $\text{H}_2\text{O}_2/\text{Si}$ molar ratio of 1.03. The open end of the plastic tube going from the syringe was immersed into the suspension with Si particles.

After the etching finished, porous Si particles were washed in Büchner-style funnel on a 55 mm diameter Grade 2 Whatman® filter. After the etching solution was removed, porous Si particles were washed three times on the filter using deionized water. Next, about 10 ml of n-pentane ($\geq 99\%$, VWR Chemicals) was poured on the filter with porous powder and it was allowed to dry for a few min under the fume hood. N-pentane reduced the surface tension of water inside the pores and prevented the collapse of porous structure during the final drying which was completed overnight in 65 °C oven. Obtained microscale PSi powders were then stored in a glass vials.

Surface oxidation and preparation of nanoparticles

After LL-MACE surfaces of PSi powders were hydrogen terminated (Figures ?? and ??, Supp. Inf.). P_b localized electronic defects were formed in the Si/SiO₂ interface using thermal

oxidation of PSi surfaces, as it was shown to give the highest number of P_b defects among other methods.³⁹ Thermal oxidation was done in NaberTherm R50/500/12 tube furnace (Nabertherm GmbH) at 345 °C in air.³⁹

Thermally oxidized PSi powders were then milled into NPs using a dedicated system.⁴¹ About 400 mg of a PSi powder was placed into a 4 ml glass vial which was subsequently filled with 1 mm ZrO_2 milling balls. The milling was then performed in 5 min cycles at 900 rpm to avoid overheating and leaks. After each cycle, pressure was released from the vials. Typically, 10 cycles were enough to obtain PSi NPs with most of the particles below 200 nm in hydrodynamic diameter (Fig. 1b).

In addition to thermal oxidation, two-step liquid-phase oxidation (oxidation in H_2O_2/NH_4OH solution followed by oxidation in H_2O_2/HCl solution),³⁹ or one-step (only H_2O_2/HCl solution) was performed for thermally oxidized PSi NPs (*i.e.*, after milling of thermally oxidized PSi powders, details in Supp. Inf.). Liquid-phase oxidation removed the remaining hydrogen in $-O_ySiH_x$ groups (Figures ?? and ??, Supp. Inf.) as well as induced additional backbond oxidation. Liquid-phase oxidation was tested because it would be needed in future surface modification with PEG molecules to prolong the systemic circulation time and enabling the use of the PSi NPs e.g. as MRI imaging contrast agents.⁴⁰

Au removal

The absence of Au NPs influence on the DNP was confirmed with the N sample. Au NPs were dissolved using the KI/I_2 gold etchant for the porous Si powder after LL-MACE. Gold etchant solution was prepared by dissolving 6.08 g of KI and 1.51 g of I_2 in 30 ml of 5 M HCl. Use of HCl as solvent demonstrated better Au dissolution compared to water. To dissolve Au NPs, about 250 mg of N powder after LL-MACE was dispersed in 3 ml of ethanol to wet the hydrophobic surfaces. Then, 15 ml of gold etchant was slowly added to the Si powder suspension. Particles were then stirred for 2 h at 75 °C. Au amount before and after the dissolution was measured using a home build portable XRF setup⁸⁶ and calculated using

the calibration standards prepared with Au deposition step of LL-MACE. Finally, particles were washed 3 times with water in a Büchner-style funnel, wetted with n-pentane and dried in an oven as above. Then the powder was milled to NPs and denoted as N-Au.

Characterization

Morphology of PSi NPs was examined by transmission electron microscopy (JEOL JEM-2100F, JEOL Ltd.). A 2.5 μl drop of suspension diluted in ethanol to a concentration of 20 $\mu\text{g}\cdot\text{ml}^{-1}$ was dried on 400 mesh Cu holey carbon grid (Agar Scientific Ltd.) and the grid was examined in the instrument. Hydrodynamic sizes of PSi NP were measured using dynamic light scattering (Zetasizer Nano ZS, Malvern Panalytical Ltd) after redispersing in water at 0.1 $\text{mg}\cdot\text{ml}^{-1}$ concentration.

Specific surface area, specific pore volume and pore size distributions of Si powders after LL-MACE were characterized by N_2 sorption (Tristar II, Micromeritics Instrument Corp.). Specific surface areas were calculated from the linear part of adsorption isotherm using Brunauer-Emmett-Teller theory. Specific pore volumes were obtained from the total adsorbed amount at relative pressure of 0.97. Pore size distributions were calculated from desorption isotherm using Barrett-Joyner-Halenda model.

Crystalline sizes of pore walls in PSi powders were estimated using X-ray powder diffraction (D8 Discover, Bruker Corp.). Powders were placed on a zero-background holder and scanned in 25 – 60° two-theta angle range with step size of 0.0057° and time per step of 0.205 s. Crystalline sizes of two Si phases and one Au phase were then calculated with Rietveld refinement method using TOPAS® 4.6 software (Section ??, Supp. Inf.).

Surface chemical species and P_b centers formed by oxidation were studied with Fourier-transform infrared spectroscopy (FTIR, Thermo Nicolet iS50, ThermoFisher Scientific Corp.) and electron paramagnetic resonance spectroscopy (ESR, Magnettech MiniScope MS5000, Bruker Corp.). In FTIR, KBr tablets with dried PSi NPs were measured in the transmission mode (Supp. Inf.). In ESR, dried PSi NP powder was poured into an ESR tube

in order to fill it at the level of 7 mm from the bottom. The tube was placed in the spectrometer at the same height for each measurement with the following parameters: (1) $B_0 = 336 \text{ mT}$, $B_0^{\text{scan}} = 15.5 \text{ mT}$, $B_0^{\text{modulation}} = 0.2 \text{ mT}$, $t_{\text{scan}} = 60 \text{ s}$, MW attenuation 25 dB and gain 10 for the full spectra; (2) $B_0 = 336 \text{ mT}$, $B_0^{\text{scan}} = 35 \text{ mT}$, $B_0^{\text{modulation}} = 0.7 \text{ mT}$, $t_{\text{scan}} = 60 \text{ s}$ averaged 3 times, MW attenuation 15 dB and gain 500 to resolve hyperfine peaks. Calculation of the P_b centers concentration and g -factor correction was done using the standard 2,2,6,6-tetramethylpiperidinyloxy (TEMPO) radical (99%, Sigma-Aldrich) sample with known number of paramagnetic centers and g -factors. ESR spectra were fitted using EasySpin 5.2.35 by simulating solid-state continuous-wave powder spectra using combination of anisotropic (111) P_b and isotropic center P_b^{iso} including g -factor strain, hyperfine constants and Voigt line broadening correspondingly (Section ??, Supp. Inf.)⁵⁶

Dynamic nuclear polarization

Hyperpolarization of PSi NPs was studied using three different polarizer designs: SpinAligner (Polarize ApS) operating at 3.35 T and 6.7 T (1.4 K), and two home-built setups relying on either OpenCore NMR operating at 3.34 T (3.4 K)⁸⁷ or a Bruker Avance III spectrometer at 7 T (3.4 K).⁵¹ About 100 mg of dried PSi NPs powder was packed into a plastic cuvette and placed in the polarizer in the SpinAligner compared to 50-60 mg for home-built set-ups. Microwave irradiation was delivered through a waveguide elbow to directly irradiate the sample. Microwave radiation^{9,26} was frequency modulated in all polarizers using a symmetric ramp function. Magnetic field strength, temperature, microwave power W , frequency modulation bandwidth $\Delta\nu_{\text{MW}}$ and frequency of modulation ν_{MW} are summarized in Tbl. 2.

NMR signal from ^{29}Si nuclei was measured with $\sim 2.8^\circ$ flip angle in the SpinAligner with varied time intervals between the measurements. Flip angles of $\sim 1.5^\circ$ each 20 min at 3.34 T and $\sim 6.9^\circ$ every 6 to 10 min at 7 T were used. Obtained data was analyzed using MATLAB scripts, where either the real part of the time-domain free induction decay (FID) was fitted with an exponential ansatz or the real part after fast Fourier transform (FFT)

in the frequency-domain was fitted with pseudo-Voigt functions. Polarization enhancements and absolute polarization values were calculated from the thermal equilibrium signal taken in the hyperpolarization conditions after 72 h of polarization with microwave radiation switched off for the 6.7 T (1.4 K) measurements (Sec. ??, Supp. Inf.). For the 3.34 and 7 T (3.4 K) measurements, the thermal equilibrium signal at 300 K of a fully ^{29}Si isotope labeled sample was measured and adjusted for temperature upon calculation of enhancements and absolute polarization in the DNP experiments. Both the polarization buildup data and the relaxation data was corrected for the effect of RF pulses used to monitor the polarization⁵² (except for the 3.34 T owing to the small flip angle used and difficulties in measuring such small flip angles with high relative accuracy).

Acknowledgement

Academy of Finland projects #314551, #331371 and #322006 are acknowledged. The microscopy studies were performed using the facilities of SIB Labs, Laboratory of Microscopy at the University of Eastern Finland. Part of the work was carried out with the support of Kuopio Biomedical Imaging Unit, University of Eastern Finland, Kuopio, Finland (part of Biocenter Kuopio, Finnish Biomedical Imaging Node, and EuroBioImaging). Silicon was provided by Elkem Silicon Products (Elkem ASA, Norway) and Okmetic (Okmetik Oy, Finland). This research has been supported by the ETH Zürich and the Schweizerischer Nationalfonds zur Förderung der Wissenschaftlichen Forschung (grant nos. 200020_188988 and 200020_219375).

Supporting Information Available

Supporting information contains the FTIR, XRPD, EPR characterization data for all the samples as well as the additional DNP data including DNP sweep spectra, polarization buildup and decay data, rate constants for various experimental conditions.

References

- (1) Dumoulin, S. O.; Fracasso, A.; van der Zwaag, W.; Siero, J. C.; Petridou, N. Ultra-high field MRI: Advancing systems neuroscience towards mesoscopic human brain function. *NeuroImage* **2018**, *168*, 345–357.
- (2) Zhong, Z.; Sun, K.; Dan, G.; Luo, Q.; Zhou, X. J. MRI with sub-millisecond temporal resolution over a reduced field of view. *Magnetic Resonance in Medicine* **2021**, *86*, 3166–3174.
- (3) Rudie, J. D.; Gleason, T.; Barkovich, M. J.; Wilson, D. M.; Shankaranarayanan, A.; Zhang, T.; Wang, L.; Gong, E.; Zaharchuk, G.; Villanueva-Meyer, J. E. Clinical Assessment of Deep Learning–based Super-Resolution for 3D Volumetric Brain MRI. *Radiology: Artificial Intelligence* **2022**, *4*, e210059.
- (4) Deoni, S. C. L.; Medeiros, P.; Deoni, A. T.; Burton, P.; Beauchemin, J.; D’Sa, V.; Boskamp, E.; By, S.; McNulty, C.; Mileski, W.; Welch, B. E.; Huentelman, M. Development of a mobile low-field MRI scanner. *Scientific Reports 2022 12:1* **2022**, *12*, 1–9.
- (5) Day, S. E.; Kettunen, M. I.; Gallagher, F. A.; Hu, D.-E.; Lerche, M.; Wolber, J.; Golman, K.; Ardenkjaer-Larsen, J. H.; Brindle, K. M. Detecting tumor response to treatment using hyperpolarized ^{13}C magnetic resonance imaging and spectroscopy. *Nature Medicine* **2007**, *13*, 1382–1387.
- (6) Gallagher, F. A.; Kettunen, M. I.; Day, S. E.; Hu, D.-E.; Ardenkjær-Larsen, J. H.; Zandt, R.; Jensen, P. R.; Karlsson, M.; Golman, K.; Lerche, M. H.; Brindle, K. M. Magnetic resonance imaging of pH in vivo using hyperpolarized ^{13}C -labelled bicarbonate. *Nature* **2008**, *453*, 940–943.
- (7) Jiang, W.; Lumata, L.; Chen, W.; Zhang, S.; Kovacs, Z.; Sherry, A. D.; Khemtong, C.

- Hyperpolarized ^{15}N -pyridine Derivatives as pH-Sensitive MRI Agents. *Scientific Reports* 2015 5:1 **2015**, 5, 1–6.
- (8) Cassidy, M. C.; Chan, H. R.; Ross, B. D.; Bhattacharya, P. K.; Marcus, C. M. In vivo magnetic resonance imaging of hyperpolarized silicon particles. *Nature Nanotechnology* **2013**, 8, 363–368.
- (9) Kwiatkowski, G.; Jähnig, F.; Steinhäuser, J.; Wespi, P.; Ernst, M.; Kozerke, S. Nanometer size silicon particles for hyperpolarized MRI. *Scientific Reports* **2017**, 7, 7946.
- (10) Seo, H.; Choi, I.; Whiting, N.; Hu, J.; Luu, Q. S.; Pudakalakatti, S.; McCowan, C.; Kim, Y.; Zacharias, N.; Lee, S.; Bhattacharya, P.; Lee, Y. Hyperpolarized Porous Silicon Nanoparticles: Potential Theragnostic Material for ^{29}Si Magnetic Resonance Imaging. *ChemPhysChem* **2018**, 19, 2143–2147.
- (11) Santos, H. In *Porous silicon for biomedical applications*, 2nd ed.; Santos, H., Ed.; Woodhead Publishing, 2021.
- (12) Wenckebach, W. T. *Essentials of Dynamic Nuclear Polarisation*; Spindrift Publications, 2016.
- (13) Hayashi, H.; Itahashi, T.; Itoh, K. M.; Vlasenko, L. S.; Vlasenko, M. P. Dynamic nuclear polarization of ^{29}Si nuclei in isotopically controlled phosphorus doped silicon. *Physical Review B* **2009**, 80, 1–10.
- (14) Dementyev, A. E.; Cory, D. G.; Ramanathan, C. High-field Overhauser dynamic nuclear polarization in silicon below the metal-insulator transition. *Journal of Chemical Physics* **2011**, 134.
- (15) Järvinen, J.; Zvezdov, D.; Ahokas, J.; Sheludyakov, S.; Vainio, O.; Lehtonen, L.; Vasiliev, S.; Fujii, Y.; Mitsudo, S.; Mizusaki, T.; Gwak, M.; Lee, S.; Lee, S.; Vlasenko, L.

- Microscopic control of ^{29}Si nuclear spins near phosphorus donors in silicon. *Physical Review B* **2015**, *92*, 2–5.
- (16) Järvinen, J.; Zvezdov, D.; Ahokas, J.; Sheludiakov, S.; Lehtonen, L.; Vasiliev, S.; Vlasenko, L.; Ishikawa, Y.; Fujii, Y. Dynamic nuclear polarization and ESR hole burning in As doped silicon. *Physical Chemistry Chemical Physics* **2020**, *22*, 10227–10237.
- (17) Dluhy, P.; Salvail, J. Z.; Saeedi, K.; Thewalt, M. L.; Simmons, S. Switchable resonant hyperpolarization transfer to ^{29}Si spins in natural silicon. *Physical Review B* **2015**, *91*, 1–5.
- (18) Luttinger, J. M. Quantum theory of cyclotron resonance in semiconductors. *Physical Review* **1956**, *102*, 1030–1041.
- (19) Feher, G.; Hensel, J. C.; Gere, E. A. Paramagnetic resonance absorption from acceptors in silicon. *Physical Review Letters* **1960**, *5*, 309–311.
- (20) Henstra, A.; Dirksen, P.; Wenckebach, W. T. Enhanced dynamic nuclear polarization by the integrated solid effect. *Physics Letters A* **1988**, *134*, 134–136.
- (21) Dirksen, P.; Henstra, A.; Wenckebach, W. T. An ESR hole burning study of dynamic nuclear polarisation of ^{29}Si in Si:B. *Journal of Physics: Condensed Matter* **1989**, *1*, 8535–8541.
- (22) Stutzmann, M.; Biegelsen, D. K. Microscopic nature of coordination defects in amorphous silicon. *Physical Review B* **1989**, *40*, 9834–9840.
- (23) Poindexter, E. H.; Gerardi, G. J.; Rueckel, M. E.; Caplan, P. J.; Johnson, N. M.; Biegelsen, D. K. Electronic traps and Pb centers at the Si/SiO₂ interface: Band-gap energy distribution. *Journal of Applied Physics* **1984**, *56*, 2844–2849.
- (24) Stesmans, A. Comparison of the low-temperature esr properties of Pb₀ defects residing

- at the interfaces of differently-oxidized Si/SiO₂ structures. *Zeitschrift für Physikalische Chemie* **1987**, *151*, 191–209.
- (25) Brower, K. L. Electron paramagnetic resonance studies of Si-SiO₂ interface defects. *Semiconductor Science and Technology* **1989**, *4*, 970–979.
- (26) Kwiatkowski, G.; Polyhach, Y.; Jähnig, F.; Shiroka, T.; Starsich, F. H. L.; Ernst, M.; Kozerke, S. Exploiting Endogenous Surface Defects for Dynamic Nuclear Polarization of Silicon Micro- and Nanoparticles. *The Journal of Physical Chemistry C* **2018**, *122*, 25668–25680.
- (27) Whiting, N.; Hu, J.; Zacharias, N. M.; Lokesh, G. L. R.; Volk, D. E.; Menter, D. G.; Rupaimoole, R.; Previs, R.; Sood, A. K.; Bhattacharya, P. Developing hyperpolarized silicon particles for *in vivo* MRI targeting of ovarian cancer. *Journal of Medical Imaging* **2016**, *3*, 036001.
- (28) Kwiatkowski, G.; Jähnig, F.; Steinhauser, J.; Wespi, P.; Ernst, M.; Kozerke, S. Direct hyperpolarization of micro- and nanodiamonds for bioimaging applications - Considerations on particle size, functionalization and polarization loss. *Journal of Magnetic Resonance* **2018**, *286*, 42–51.
- (29) Boele, T.; Waddington, D. E.; Gaebel, T.; Rej, E.; Hasija, A.; Brown, L. J.; McCamey, D. R.; Reilly, D. J. Tailored nanodiamonds for hyperpolarized C 13 MRI. *Physical Review B* **2020**, *101*, 1–11.
- (30) Atkins, T. M.; Cassidy, M. C.; Lee, M.; Ganguly, S.; Marcus, C. M.; Kauzlarich, S. M. Synthesis of Long-T1 Silicon Nanoparticles for Hyperpolarized ²⁹Si Magnetic Resonance Imaging. *ACS Nano* **2013**, *7*, 1609–1617.
- (31) Tamarov, K.; Swanson, J. D.; Unger, B. A.; Kolasinski, K. W.; Ernst, A. T.; Aindow, M.; Lehto, V.-P.; Riikonen, J. Controlling the nature of etched Si nanostructures:

- High versus low load metal-assisted catalytic etching (MACE) of Si powders. *ACS Applied Materials & Interfaces* **2020**, *12*, 4787–4796.
- (32) Tamarov, K.; Kiviluoto, R.; Swanson, J.; Unger, B.; Ernst, A.; Aindow, M.; Riikonen, J.; Lehto, V.-P.; Kolasinski, K. Low-Load Metal-Assisted Catalytic Etching Produces Scalable Porosity in Si Powders. *ACS Applied Materials & Interfaces* **2020**, *12*, 48969–48981.
- (33) Aptekar, J. W. et al. Silicon nanoparticles as hyperpolarized magnetic resonance imaging agents. *ACS Nano* **2009**, *3*, 4003–4008.
- (34) Kim, J.; Jo, D.; Yang, S.-H.; Joo, C.-G.; Whiting, N.; Pudakalakatti, S.; Seo, H.; Son, H. Y.; Min, S.-J.; Bhattacharya, P.; Huh, Y.-M.; Shim, J. H.; Lee, Y. ^{29}Si Isotope-Enriched Silicon Nanoparticles for an Efficient Hyperpolarized Magnetic Resonance Imaging Probe. *ACS Applied Materials & Interfaces* **2021**, *13*, 56923–56930.
- (35) Hu, J.; Whiting, N.; Bhattacharya, P. Hyperpolarization of Silicon Nanoparticles with TEMPO Radicals. *The Journal of Physical Chemistry C* **2018**, *122*, 10575–10581.
- (36) Klaassen, D. B. M. A unified mobility model for device simulation—I. Model equations and concentration dependence. *Solid-State Electronics* **1992**, *35*, 961–967.
- (37) Koiller, B.; Hu, X.; Das Sarma, S.; Koiller, B. Exchange in Silicon-Based Quantum Computer Architecture. *Physical Review Letters* **2002**, *88*, 4.
- (38) Chandrasekhar, S. Stochastic problems in physics and astronomy. *Reviews of Modern Physics* **1943**, *15*, 1–89.
- (39) Riikonen, J.; Salomäki, M.; Van Wonderen, J.; Kemell, M.; Xu, W.; Korhonen, O.; Ritala, M.; MacMillan, F.; Salonen, J.; Lehto, V. P. Surface chemistry, reactivity, and pore structure of porous silicon oxidized by various methods. *Langmuir* **2012**, *28*, 10573–10583.

- (40) Nissinen, T.; Näkki, S.; Laakso, H.; Kučiauskas, D.; Kaupinis, A.; Kettunen, M. I.; Liimatainen, T.; Hyvönen, M.; Valius, M.; Gröhn, O.; Lehto, V. P. Tailored Dual PEGylation of Inorganic Porous Nanocarriers for Extremely Long Blood Circulation in Vivo. *ACS Applied Materials & Interfaces* **2016**, *8*, 32723–32731.
- (41) Nissinen, T.; Ikonen, T.; Lama, M.; Riikonen, J.; Lehto, V.-P. Improved production efficiency of mesoporous silicon nanoparticles by pulsed electrochemical etching. *Powder Technology* **2016**, *288*, 360–365.
- (42) Born, M.; Wolf, E. *Principles of Optics*, 60th ed.; Cambridge University Press, 2019.
- (43) Von Bardeleben, H. J.; Schoisswohl, M.; Cantin, J. L. Electron paramagnetic resonance study of defects in oxidized and nitrided porous Si and Si(1-x)Ge(x). *Colloids and Surfaces A: Physicochemical and Engineering Aspects* **1996**, *115*, 277–289.
- (44) Stesmans, A.; Afanas'ev, V. V. Electron spin resonance features of interface defects in thermal (100) Si/SiO₂. *Journal of Applied Physics* **1998**, *83*, 2449–2457.
- (45) Poindexter, E. H.; Caplan, P. J. Characterization of Si/SiO₂ interface defects by electron spin resonance. *Progress in Surface Science* **1983**, *14*, 201–294.
- (46) Rong, F. C.; Harvey, J. F.; Poindexter, E. H.; Gerardi, G. J. Nature of Pb-like dangling-orbital centers in luminescent porous silicon. *Applied Physics Letters* **1993**, *63*, 920–922.
- (47) von Bardeleben, H. J.; Chamarro, M.; Grosman, A.; Morazzani, V.; Ortega, C.; Siejka, J.; Rigo, S. Pb-defects and visible photoluminescence in porous silicon. *Journal of Luminescence* **1993**, *57*, 39–43.
- (48) Von Bardeleben, H. J.; Stievenard, D.; Grosman, A.; Ortega, C.; Siejka, J. Defects in porous p-type Si: An electron-paramagnetic-resonance study. *Physical Review B* **1993**, *47*, 10899–10902.

- (49) Laiho, R.; Vlasenko, L. S.; Afanasiev, M. M.; Vlasenko, M. P. Electron paramagnetic resonance in heat-treated porous silicon. *Journal of Applied Physics* **1994**, *76*, 4290–4293.
- (50) Stoll, S.; Schweiger, A. EasySpin, a comprehensive software package for spectral simulation and analysis in EPR. *Journal of Magnetic Resonance* **2006**, *178*, 42–55.
- (51) Himmler, A.; Albannay, M. M.; Von Witte, G.; Kozerke, S.; Ernst, M. Electroplated waveguides to enhance DNP and EPR spectra of silicon and diamond particles. *Magnetic Resonance* **2022**, *3*, 203–209.
- (52) Witte, G. V.; Ernst, M.; Kozerke, S. Modelling and correcting the impact of RF pulses for continuous monitoring of hyperpolarized NMR. *Magnetic Resonance* **2023**, 1–16.
- (53) Dementyev, A. E.; Cory, D. G.; Ramanathan, C. Dynamic Nuclear Polarization in Silicon Microparticles. *Physical Review Letters* **2008**, *100*, 127601.
- (54) Rej, E.; Gaebel, T.; Boele, T.; Waddington, D. E.; Reilly, D. J. Hyperpolarized nanodiamond with long spin-relaxation times. *Nature Communications* **2015**, *6*, 1–7.
- (55) Rong, F. C.; Harvey, J. F.; Poindexter, E. H.; Gerardi, G. J. Identification and Properties of Pb-like Centers in Photoluminescent Porous Silicon. *Microelectronic Engineering* **1993**, *22*, 147–150.
- (56) Konstantinova, E. A. In *Handbook of Porous Silicon*, 2nd ed.; Canham, L. T., Ed.; Springer International Publishing, 2018; pp 627–654.
- (57) Bertrand, P. *Electron Paramagnetic Resonance Spectroscopy Fundamentals*; Springer Cham, 2020.
- (58) Brower, K. L.; Headley, T. Dipolar interactions between dangling bonds at the (111) Si-SiO₂ interface. *Physical Review B* **1986**, *34*, 3610–3619.

- (59) Meyer, B. K.; Petrova-Koch, V.; Muschik, T.; Linke, H.; Omling, P.; Lehmann, V. Electron spin resonance investigations of oxidized porous silicon. *Applied Physics Letters* **1993**, *63*, 1930–1932.
- (60) Young, C. F.; Poindexter, E. H.; Gerardi, G. J. Electron paramagnetic resonance of porous silicon : Observation and identification of conduction-band electrons. *Journal of Applied Physics* **1997**, *81*, 7468–7470.
- (61) Stesmans, A.; Van Gorp, G. Observation of dipolar interactions between Pb0 defects at the (111) Si/SiO₂ interface. *Physical Review B* **1990**, *42*, 3765–3768.
- (62) Gorp, V.; Stesmans, A. Dipolar interaction between [111] Pb defects at the (111)Si/SiO₂ interface revealed by electron-spin resonance. *Physical Review B* **1992**, *45*, 4344–4371.
- (63) Iacovo, S.; Stesmans, A. Inherent interface defects in thermal (211)Si/SiO₂:²⁹Si hyperfine interaction. **2014**, *1624*, 49–57.
- (64) Xiao, Y.; McMahon, T. J.; Pankove, J. I.; Tsuo, Y. S. Existence of a Pb1-like defect center in porous silicon. *Journal of Applied Physics* **1994**, *76*, 1759–1763.
- (65) Stesmans, A.; Afanas'ev, V. V. Undetectability of the Pb1 point defect as an interface state in thermal (100)Si/SiO₂. *Journal of Physics Condensed Matter* **1998**, *10*.
- (66) Braet, J.; Stesmans, A. Low T characterization of the Pbo- defect spin relaxation at (111) Si/SiO₂ interfaces. *Physica B+C* **1984**, *126*, 463–464.
- (67) Kundu, K.; Feintuch, A.; Vega, S. Theoretical Aspects of the Cross Effect Enhancement of Nuclear Polarization under Static Dynamic Nuclear Polarization Conditions. *Journal of Physical Chemistry Letters* **2019**, *10*, 1769–1778.
- (68) Venkatesh, A.; Casano, G.; Rao, Y.; De Biasi, F.; Perras, F. A.; Kubicki, D. J.; Siri, D.; Abel, S.; Karoui, H.; Yulikov, M.; Ouari, O.; Emsley, L. Deuterated TEKPol Biradi-

- cals and the Spin-Diffusion Barrier in MAS DNP. *Angewandte Chemie - International Edition* **2023**, *62*, e202304844.
- (69) Wenckebach, W. T. Dynamic nuclear polarization via the cross effect and thermal mixing: A. The role of triple spin flips. *Journal of Magnetic Resonance* **2019**, *299*, 124–134.
- (70) Wenckebach, W. T. Dynamic nuclear polarization via the cross effect and thermal mixing: B. Energy transport. *Journal of Magnetic Resonance* **2019**, *299*, 151–167.
- (71) Wenckebach, W. T. Electron Spin–Spin Interactions in DNP: Thermal Mixing vs. the Cross Effect. *Applied Magnetic Resonance* **2021**, *52*, 731–748.
- (72) Wenckebach, W. T.; Capozzi, A.; Patel, S.; Ardenkjær-Larsen, J. H. Direct measurement of the triple spin flip rate in dynamic nuclear polarization. *Journal of Magnetic Resonance* **2021**, *327*.
- (73) Wenckebach, W. T.; Quan, Y. Monte Carlo study of the spin-spin interactions between radicals used for dynamic nuclear polarization. *Journal of Magnetic Resonance* **2021**, *326*, 106948.
- (74) Wenckebach, W.; Cox, S. Nuclear dipolar relaxation induced by interacting ground state electron spins. *Journal of Magnetic Resonance* **2023**, *348*, 107375.
- (75) Lee, M.; Cassidy, M. C.; Ramanathan, C.; Marcus, C. M. Decay of nuclear hyperpolarization in silicon microparticles. *Physical Review B - Condensed Matter and Materials Physics* **2011**, *84*, 33–35.
- (76) Hovav, Y.; Feintuch, A.; Vega, S.; Goldfarb, D. Dynamic nuclear polarization using frequency modulation at 3.34 T. *Journal of Magnetic Resonance* **2014**, *238*, 94–105.
- (77) Bloembergen, N. On the interaction of nuclear spins in a crystalline lattice. *Physica* **1949**, *15*, 386–426.

- (78) Horvitz, E. P. Nuclear spin diffusion induced by paramagnetic impurities in nonconducting solids. *Physical Review B* **1971**, *3*, 2868–2872.
- (79) Wittmann, J. J.; Eckardt, M.; Harneit, W.; Corzilius, B. Electron-driven spin diffusion supports crossing the diffusion barrier in MAS DNP. *Physical Chemistry Chemical Physics* **2018**, *20*, 11418–11429.
- (80) Stern, Q.; Cousin, S. F.; Mentink-vigier, F.; Pinon, A. C.; Elliott, S. J.; Cala, O.; Jannin, S. Direct observation of hyperpolarization breaking through the spin diffusion barrier. *Science Advances* **2021**, *7*, 1–13.
- (81) Chessari, A.; Cousin, S. F.; Jannin, S.; Stern, Q. The role of electron polarization on nuclear spin diffusion. *Physical Review B* **2023**, *107*, 224429.
- (82) Prisco, N. A.; Pinon, A. C.; Emsley, L.; Chmelka, B. F. Scaling analyses for hyperpolarization transfer across a spin-diffusion barrier and into bulk solid media. *Physical Chemistry Chemical Physics* **2021**, *23*, 1006–1020.
- (83) von Witte, G.; Himmler, A.; Kozerke, S.; Ernst, M. Relaxation enhancement by microwave irradiation may limit dynamic nuclear polarization. 2023; <http://arxiv.org/abs/2312.07244>, arXiv:2312.07244 [physics].
- (84) Abragam, A.; Goldman, M. *Nuclear Magnetism: Order and Disorder*; Oxford University Press, 1982.
- (85) Sailor, M. J. *Porous silicon in practice: preparation, characterization and applications*; 2012; p 262.
- (86) Tiihonen, T. E.; Nissinen, T. J.; Turhanen, P. A.; Vepsäläinen, J. J.; Riikonen, J.; Lehto, V. P. Real-Time On-Site Multielement Analysis of Environmental Waters with a Portable X-ray Fluorescence (pXRF) System. *Analytical Chemistry* **2022**, *94*, 11739–11744.

- (87) Batel, M.; Krajewski, M.; Weiss, K.; With, O.; Däpp, A.; Hunkeler, A.; Gimersky, M.; Pruessmann, K. P.; Boesiger, P.; Meier, B. H.; Kozerke, S.; Ernst, M. A multi-sample 94 GHz dissolution dynamic-nuclear-polarization system. *Journal of Magnetic Resonance* **2012**, *214*, 166–174.

TOC Graphic

Some journals require a graphical entry for the Table of Contents. This should be laid out “print ready” so that the sizing of the text is correct. Inside the tocentry environment, the font used is Helvetica 8 pt, as required by *Journal of the American Chemical Society*.

The surrounding frame is 9 cm by 3.5 cm, which is the maximum permitted for *Journal of the American Chemical Society* graphical table of content entries. The box will not resize if the content is too big: instead it will overflow the edge of the box.

This box and the associated title will always be printed on a separate page at the end of the document.

Supporting Information

for

Controlled synthesis and characterization of porous silicon nanoparticles for dynamic nuclear polarization

Gevin von Witte,^{†,‡} Aaron Himmler,[‡] Viivi Hyppönen,[¶] Jiri Jäntti,[§] Mohammed M. Albannay,[†] Jani O. Moilanen,^{||} Matthias Ernst,[‡] Vesa-Pekka Lehto,[§] Joakim Riikonen,[§] Sebastian Kozerke,[†] Mikko I. Kettunen,^{¶,⊥} and Konstantin Tamarov^{*,§,⊥}

[†]*Institute for Biomedical Engineering, University and ETH Zurich, Zurich, Switzerland*

[‡]*Institute of Molecular Physical Science, ETH Zurich, Zurich, Switzerland*

[¶]*Kuopio Biomedical Imaging Unit, A.I. Virtanen Institute, University of Eastern Finland, Kuopio, Finland*

[§]*Department of Technical Physics, University of Eastern Finland, Kuopio, Finland*

^{||}*Department of Chemistry, Nanoscience Center, University of Jyväskylä, Jyväskylä, Finland*

[⊥]*Joint senior authorship*

E-mail: konstantin.tamarov@uef.fi

S1 Liquid-phase oxidation

Two-step and one-step oxidation were performed for PSi NPs (*i.e.*, after milling of thermally oxidized PSi powders) according to the procedure described in ref.¹ In the first step of oxidation, about 100 mg of PSi NPs stored in ethanol suspension were first redispersed in deionized water by repeating two times the following sequence: centrifugation of PSi NP suspension, supernatant removal, redispersion in water in an ultrasound bath (Elmasonic S10). The final redispersion used only 10 ml of water. Next, 10 ml of NH_4OH (7 wt.%, VWR Chemicals) solution was slowly added under stirring followed by slow pouring of 2 ml H_2O_2 (35 wt.%, Acros Organics, Thermo Fisher GmbH). The suspension was then sonicated for 1 min and placed on heating plate and the oxidation reaction proceed for 15 min at 90 °C under stirring. The reaction was then slowed down by diluting the suspension with about 30 ml of water, and the PSi NPs were washed with water by repeating centrifugation-redispersion cycle three times. Again, the final redispersion used only 10 ml of water. In the second step of oxidation, 10 ml of 2 M HCl is added to the NPs under stirring, into which subsequently 2 ml of H_2O_2 (35 wt.%) is poured. The reaction is then carried out at 90 °C for 15 min. Finally, washing is performed as in the first step with the final replacement of water with ethanol for NP storage. One-step oxidation employed only the second step of the two-step liquid-phase oxidation.

S2 Characterization of PSi NPs

S2.1 Fourier-transform infrared spectroscopy

Surface oxidation of PSi NPs was characterized using Fourier-transform infrared spectroscopy (FTIR, Thermo Nicolet iS50) of KBr tablets. The tablets were prepared by grinding 200 mg of dried KBr powder together with 1-2 mg of dried PSi NPs in a mortar until the powder color became homogeneous. Manual hydraulic press converted the powder into a uniformly

colored KBr tablet. FTIR measurements were then performed in transmission mode.

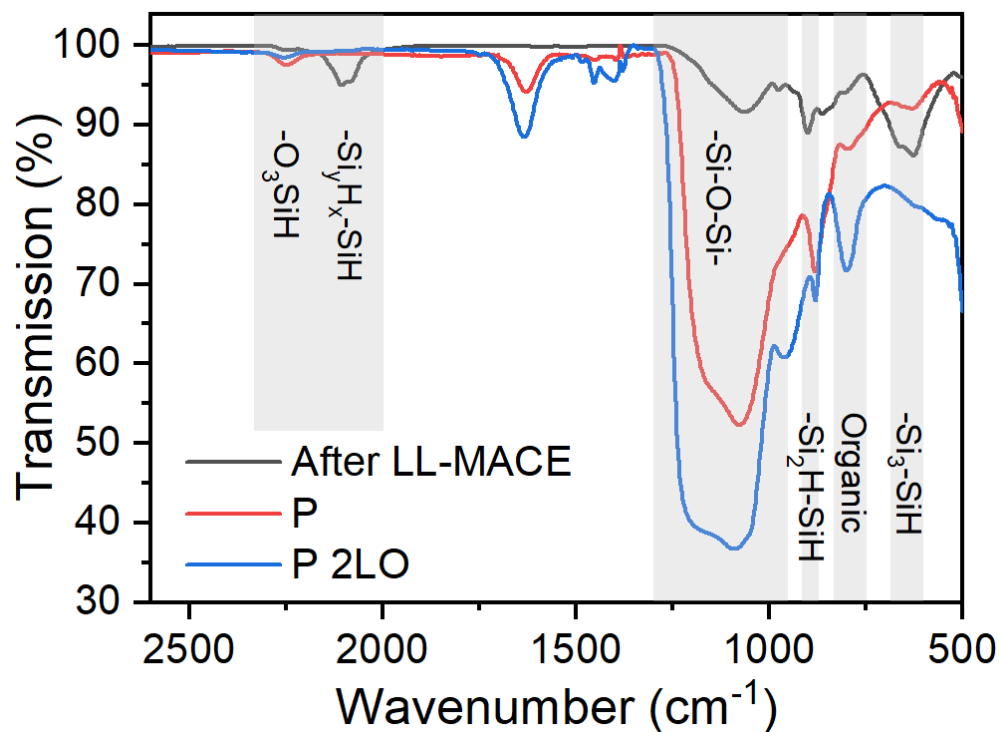


Figure S1: Transmission FTIR spectra of hydrogen-terminated P PSi powder after LL-MACE (dark line), thermally oxidized P PSi NPs (red line), and P PSi NPs after liquid and thermal oxidation (blue line). Grey shaded squares and labels assign FTIR peaks.

Figures S1 and S2 depict the difference between the hydrogen-terminated sample after LL-MACE, milled PSi NPs prepared from thermally oxidized PSi powders, and the liquid-phased oxidized PSi NPs. Hydrogen-terminated sample shows strong IR absorption peaks at 615 – 625 cm^{-1} , 948 cm^{-1} , and 2050 – 2160 cm^{-1} that correspond to various silicon hydride species on PSi surfaces.¹ The wide peak at 1000 – 1250 cm^{-1} and the peak at 2248 cm^{-1} demonstrate the native oxidation process during overnight drying in an oven at 65 °C. Thermal oxidation with subsequent milling to NPs created the strong Si–O–Si oxide peak with almost complete disappearance of $-\text{Si}_y\text{H}_x-\text{SiH}$ hydride species. However, an appearance of hydrogen bound to backbone oxidized Si was observed ($-\text{O}_3\text{SiH}$ species) indicating that not all the hydrogen was removed from PSi surfaces. The presence of hydrogen can impede surface functionalization based on reaction with silanes (for example, PEG-silanes² or amine-silanes³). Therefore,

additional liquid-phase oxidation was applied to PSi NPs to further reduce hydride species on NP surfaces, and the influence of oxidation on hyperpolarization was studied. Both two-step and one-step liquid-phase oxidations efficiently reduced the number of $-\text{Si}_y\text{H}_x-\text{SiH}$ although decreasing the gain in ^{29}Si hyperpolarization (see the main text).

Au removal involved highly oxidative iodine solution applied to the N PSi NPs after LL-MACE. The solution effectively oxidized Si surfaces as it can be seen in Fig. S2. The Si oxidative action of the Au etchant was found to be similar to other oxidation types and resulted in nearly full removal of the surface Si-H groups followed by Si backbond oxidation.¹

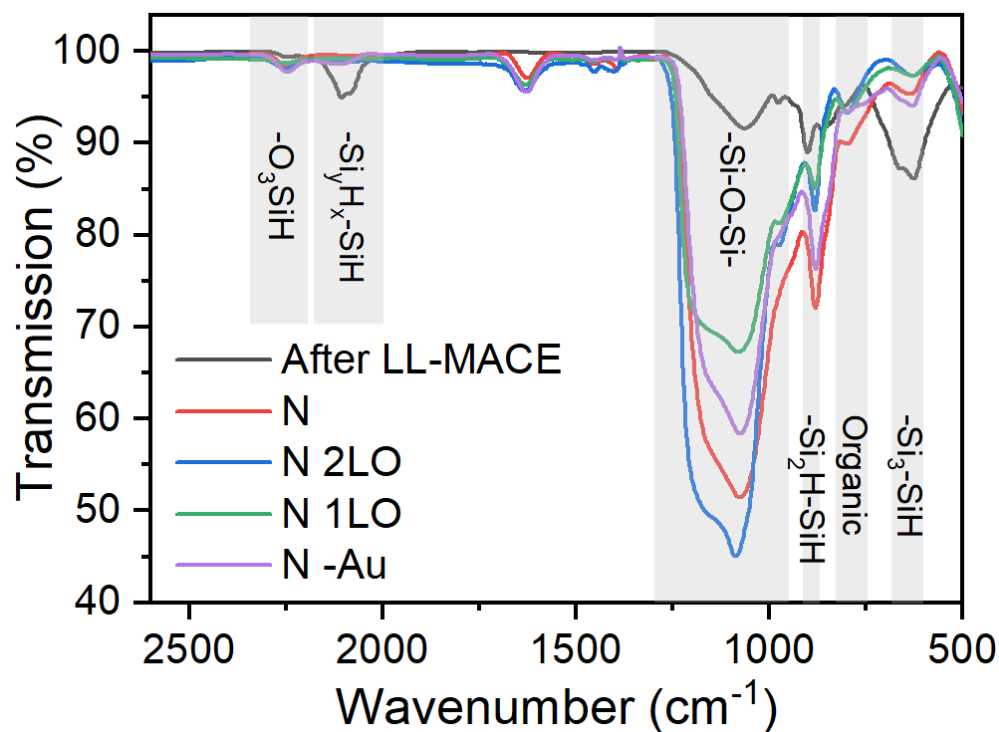


Figure S2: Transmission FTIR spectra of hydrogen-terminated N PSi powder after LL-MACE (dark line), thermally oxidized N PSi NPs (red line), N PSi NPs after two-step liquid and thermal oxidation (blue line), N PSi NPs after one-step liquid and thermal oxidation (green line), and N PSi NPs with Au removed (magenta line). Grey shaded squares and labels assign FTIR peaks.

S2.2 X-ray powder diffraction

Crystalline sizes of PSi particles after LL-MACE were calculated using Retveld refinement in TOPAS® 4.6 software. Typically, three phases were needed to correctly fit a spectrum: two Si phases and one Au phase (Fig. S3). The Si phases corresponded to the pore walls between etch track pores produced by Au NP movement, and to the pore walls between pores produced by remote etching.^{4,5}

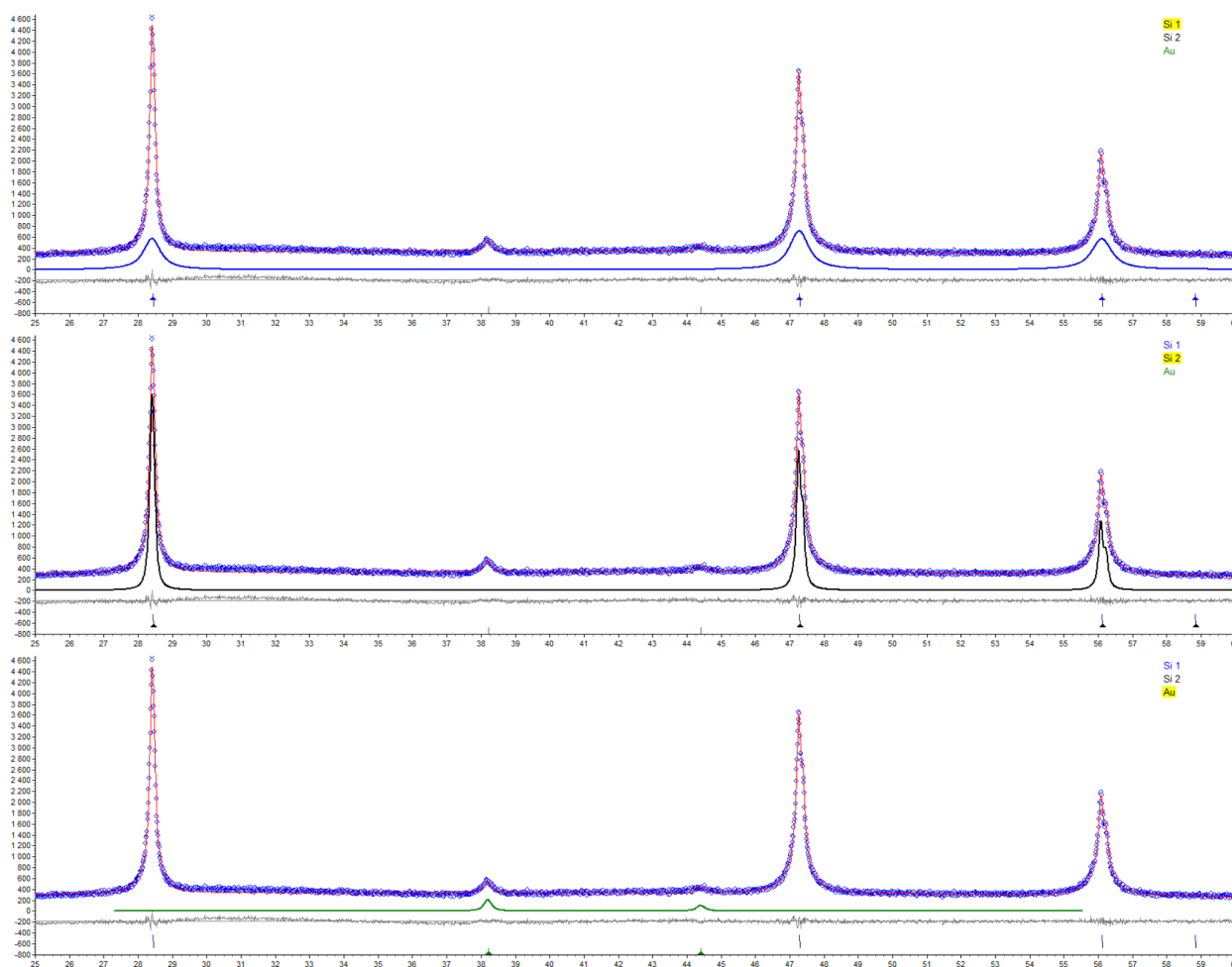


Figure S3: Fitting of XRPD spectrum of P sample with two Si phases and one Au phase. All the samples were processed in the same way.

S2.3 Electron paramagnetic resonance

Electron paramagnetic resonance (ESR) studies were performed using X-band Magnettech MiniScope MS5000 spectrometer operating at room temperature. The same volume of PSi NPs powder was placed in an ESR tube and the tube was placed at the same height for each measurement. The mass and surface number of paramagnetic centers was calculated by double integration of spectra with subsequent comparison with a TEMPO sample with a known number of radicals. The mass and surface amount of the paramagnetic centers is summarized in Table S1. The concentration of the centers per unit of mass was comparable for all the samples and ranged from $(4.4 \pm 0.4) \cdot 10^{15} \text{ mg}^{-1}$ for N+ to $(6.3 \pm 0.6) \cdot 10^{15} \text{ mg}^{-1}$ for N 1LO. The surface density for P++ and N++ samples was about 3 times smaller than for other samples due to their higher surface area (Fig. ??d) while the number of centers per unit mass remained roughly the same.

Table S1: Summary of the experimental ESR data. The number of P_b centers was calculated from the known paramagnetic center concentration of TEMPO radical and additionally confirmed using thermally oxidized electrochemically etched PSi sample.¹

Sample	Calculated from TEMPO sample		Experimental data	
	P_b centers, $\cdot 10^{15} \text{ mg}^{-1}$	P_b centers, $\cdot 10^{12} \text{ cm}^{-2}$	ESR lwpp ^a , mT	ESR FWHM ^b , mT
PSi	4.6 ± 0.4	1.9 ± 0.1	1.10	1.13
P++	5.4 ± 0.3	2.7 ± 0.1	0.76	1.03
P+	4.5 ± 0.4	5.0 ± 0.5	0.55	0.92
P	4.8 ± 0.3	5.3 ± 0.3	0.57	0.93
P 2LO	5.3 ± 0.3	5.9 ± 0.4	0.55	0.90
UW	5.2 ± 0.3	4.9 ± 0.3	0.55	0.90
N	5.6 ± 0.4	6.1 ± 0.5	0.55	0.90
N 2LO	5.4 ± 0.2	5.8 ± 0.3	0.55	0.92
N 1LO	6.3 ± 0.6	6.8 ± 0.7	0.55	0.90
N -Au	4.9 ± 0.4	5.2 ± 0.4	0.53	0.87
N+	4.4 ± 0.4	4.1 ± 0.4	0.55	0.94
N++	4.7 ± 0.4	1.8 ± 0.1	0.60	0.95
MC10	5.5 ± 0.3	3.1 ± 0.2	0.60	0.96

^a peak-to-peak linewidth ^b full width at half maximum

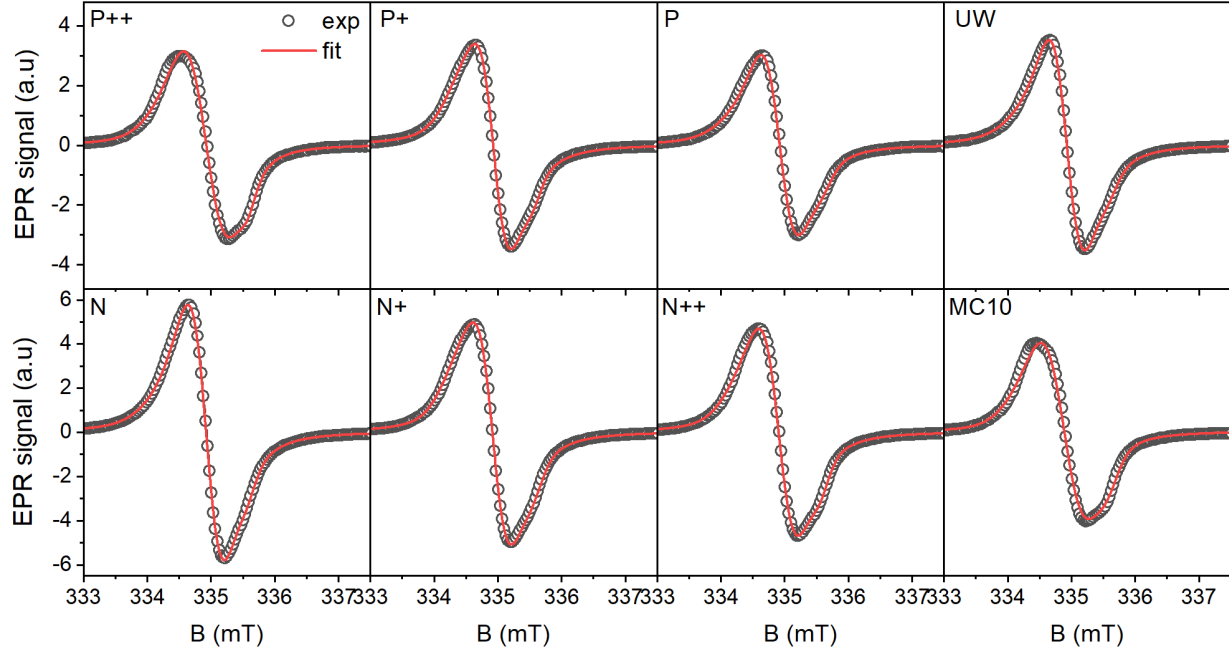


Figure S4: Electron paramagnetic resonance spectra of thermally oxidized PSi NPs of different Si types. The experimental data (dark lines) was fitted (red lines) as discussed in the text.

ESR spectra of thermally oxidized PSi NPs of different Si types and different additional liquid oxidations are presented in Figs. S4 and S5, respectively. All spectra represent a powder average of paramagnetic dangling bond P_b centers that are in turn randomly oriented and located at different Si crystalline planes in Si/SiO₂ interface.⁶ Hyperfine satellite peaks at $\Delta B = 5.8 - 7.7$ mT unambiguously demonstrated the presence of ²⁹Si nuclei at the central P_b position (Fig. S6). The hyperfine constants $A = 325 - 431$ MHz coincide well with $A_{\parallel} = 210$ MHz and $A_{\perp} = 417$ MHz for the (111) P_b center.⁷ The superhyperfine interaction typically observable for planar (111) P_b center at about 0.8 mT or 45 MHz⁸ could not be resolved due to high peak broadening in our samples but was assumed to be present.

Following the discussion of P_b centers in the main text, the measured ESR spectra were fitted with EasySpin 5.2.35⁹ using a combination of P_b^{iso} and (111) P_b , since these centers are assumed to be the dominant ones in thermally oxidized porous Si.¹⁰ The inclusion of the (111) P_b center in the fitting was the most obvious for the standard thermally oxidized porous Si sample prepared by the conventional electrochemical anodization of (100) P++ Si wafer

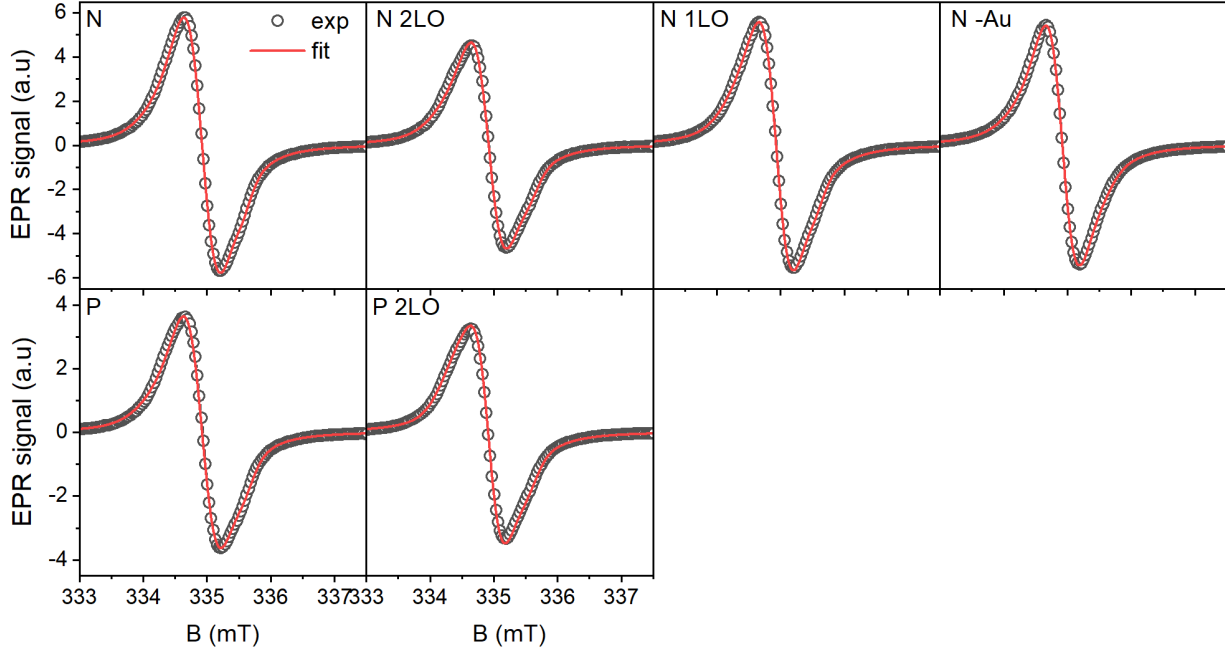


Figure S5: Electron paramagnetic resonance spectra of thermally oxidized P and N PSi NPs, after additional two-step (2LO) or one-step (1LO) liquid oxidation, or PSi NPs prepared by milling N PSi powder oxidized by gold etchant. The experimental data (dark lines) was fitted (red lines) as discussed in the text.

(Fig. S7)¹¹ with subsequent thermal oxidation. During the electrochemical anodization, the etched pores are formed normal to the (100) surface, which results in more pronounced signal from (111) P_b centers compared to much less ordered pores in the LL-MACE samples. Nevertheless, even in the LL-MACE samples the anisotropy of the ESR spectrum at about 336 mT is due to the presence of (111) P_b centers (Fig. S4 and S5).

The resulting fitting parameters for the anodized PSi sample give reasonable values. The weights for the P_b and P_b^{iso} components are 0.37 and 0.63, respectively, which show the presence of relatively high fraction of well-defined (111) P_b centers. As it is expected, the g -factor strain for $\mathbf{B} \perp [111]$ is much higher than for $\mathbf{B} \parallel [111]$ with the strain values close to the ones measured for planar (111) P_b center.¹² The Gaussian and Lorentzian peak-to-peak linewidths for the P_b are $\Delta B_{pp}^G = 0.045$ mT and $\Delta B_{pp}^L = 0.16$ mT, respectively^{13,14} (Table S2). These linewidths closely match the values evaluated by Stesmans et al.^{13,14} during their study of dipolar interaction between (111) P_b and its influence on the low-

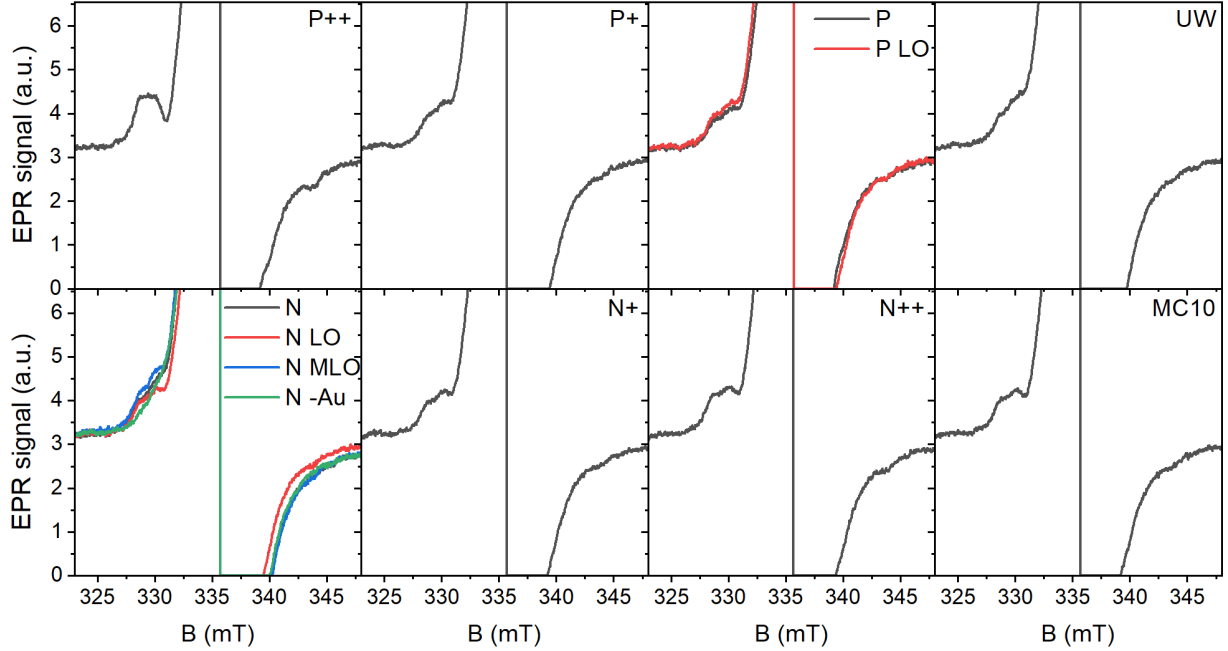


Figure S6: Electron paramagnetic resonance spectra of all the samples depicting peaks for hyperfine interaction of electron spin with the central ^{29}Si nuclei. The superhyperfine interaction with the backbond ^{29}Si nuclei is invisible due to large width of P_b^{iso} spectra.

temperature ESR spectra. Indeed, they found $\Delta B_{pp}^L \approx 0.16$ mT for $[P_b] \approx 7 \cdot 10^{12}$ cm $^{-2}$. With the weight decrease of the P_b centers in LL-MACE samples, the P_b fitting becomes less straightforward and the fitting parameters start to deviate from the ones for the planar P_b centers. This is expected due to high structural irregularity of the samples' porous surfaces.

Compared to P_b centers, P_b^{iso} was described by phenomenological Gaussian ΔB_{pp}^G and Lorentzian ΔB_{pp}^L peak-to-peak linewidths. They were found to be of the same order of magnitude in the range of 0.1 – 0.5 mT, which constituted the total linewidth of ≈ 0.6 mT and corresponded to the average linewidth of randomly oriented P_b centers found on different crystalline planes.^{12,15} The Gaussian part in the linewidth was assumed to come from the g -factor strain that was not included as an additional fitting parameter for P_b^{iso} , while the Lorentzian part showed even larger values than the ones that take into account dipolar interaction induced broadening^{13,14} (Table S2). We were not able to find a feasible explanation for such a large broadening from the porous Si literature. One possible explanation is the clustering of P_b centers due to the irregularity of the porous surface in a similar way it was

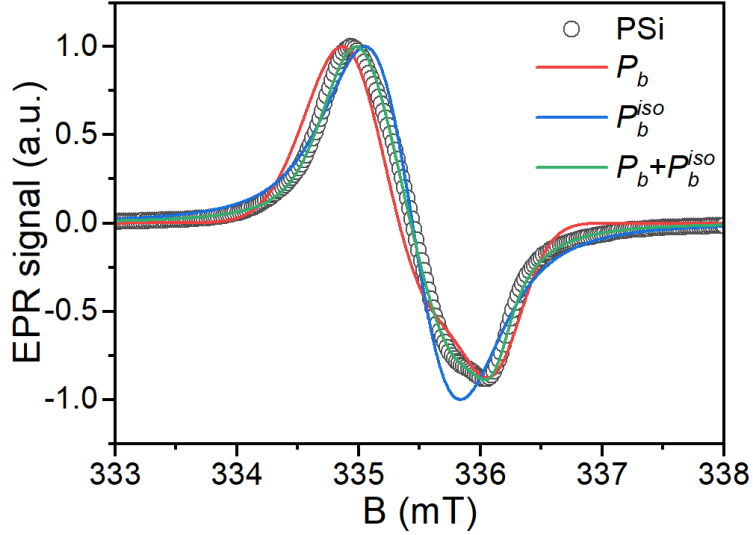


Figure S7: Fitting of the experimental ESR spectra of TOPSi sample (open dark circles) with powder pattern of (111) P_b centers (red line), P_b^{iso} centers (blue line), and combination of the two centers (green line). Obtained weights for P_b and P_b^{iso} were 0.37 and 0.63, respectively. The g strain for P_b defect was $\Delta g_{\perp} = 0.00296$ and $g_{\parallel} = 0.0005$.

demonstrated by LOD-ESR for partially amorphous Si sample.¹⁶ Overall, it is reasonable to assume the presence of dipolar interaction in our samples with similar $[P_b]$ or higher concentrations compared to Stesmans et al.^{13,14} (Table S1).

The results of EasySpin simulation of the ESR spectra were then used to calculate the ESR spectra at the DNP conditions. For this, the best fit models for each sample were fed to EasySpin to simulate powder pattern structure representing the high-field frequency-swept experimental conditions. All the high field spectra looked similar and, therefore, only the ones for P sample are presented (Fig. S8). Similar to the X-band ESR, the high-field spectra show the strong central peak and the two weak satellite peaks, which correspond to the P_b centers located on the central ^{28}Si and ^{29}Si atoms, respectively. We highlight the slight shift towards higher frequency of the strongest ESR peak compared to zero DNP frequency (Fig. S3.2) possibly due to slightly lower experimental magnetic field strength than 6.7 T used for the ESR simulation.

As a final remark, conduction band electrons with $g = 1.9995$ have been observed in

Table S2: EasySpin simulation results of the experimental ESR data. The fitting was performed according to the mixture of anisotropic $P_b^{(111)}$ and isotropic P_b^{iso} centers. Anisotropic centers were fitted with $g_{\parallel} = 2.00185$, $A_{\parallel} = 230 \pm 25$ MHz and $g_{\perp} = 2.0081$, $A_{\perp} = 420 \pm 15$ MHz with g -strain⁷ and Lorentzian line broadening¹⁴ to include g -factor stain and P_b dipolar interaction, respectively. P_b^{iso} centers were fitted with Voigtian lineshape to include homogeneous and inhomogeneous line broadening effects due to strain and dipolar interaction.

Sample	$P_b^{(111)}$				P_b^{iso}			
	$g_{\perp} \cdot 10^{-3}$ strain	$g_{\parallel} \cdot 10^{-3}$ strain	ΔB_{pp}^L , mT	weight, %	g -factor	ΔB_{pp}^G , mT	ΔB_{pp}^L , mT	weight, %
PSi	3.0	0.1	0.0012	13	2.0055	0.69	0.28	87
P++	5.4	1.3	0.0041	11	2.0054	0.46	0.37	89
P+	3.7	1.3	0.0001	9	2.0054	0.13	0.49	91
P	5.9	1.7	0.0009	11	2.0055	0.24	0.45	89
P 2LO	3.1	0.1	0.0014	11	2.0054	0.00	0.49	89
UW	5.9	1.6	0.0014	8	2.0055	0.21	0.45	92
N	5.6	1.4	0.0006	8	2.0054	0.23	0.45	92
N 2LO	5.2	1.8	0.0017	9	2.0055	0.17	0.47	91
N 1LO	4.3	1.6	0.0018	7	2.0054	0.12	0.48	93
N -Au	5.5	1.9	0.0027	4	2.0054	0.13	0.47	96
N+	3.6	0.1	0.0003	13	2.0054	0.19	0.47	87
N++	4.7	1.6	0.0009	12	2.0055	0.26	0.45	88
MC10	5.2	0.6	0.0022	15	2.0056	0.47	0.37	85

heavily doped n -type porous Si and p -type porous Si under illumination at 4.2 K.^{17,18} It is, however, not possible to identify conduction band electrons in our samples. Although the fitting of ESR does give the g -factor close to 1.9995 (Fig. S9), the peak width is at least three times larger than 0.1 mT measured by Young et al.^{17,18} Thus, it is concluded that neither conduction band electrons nor the phosphorus donor electrons could be identified.

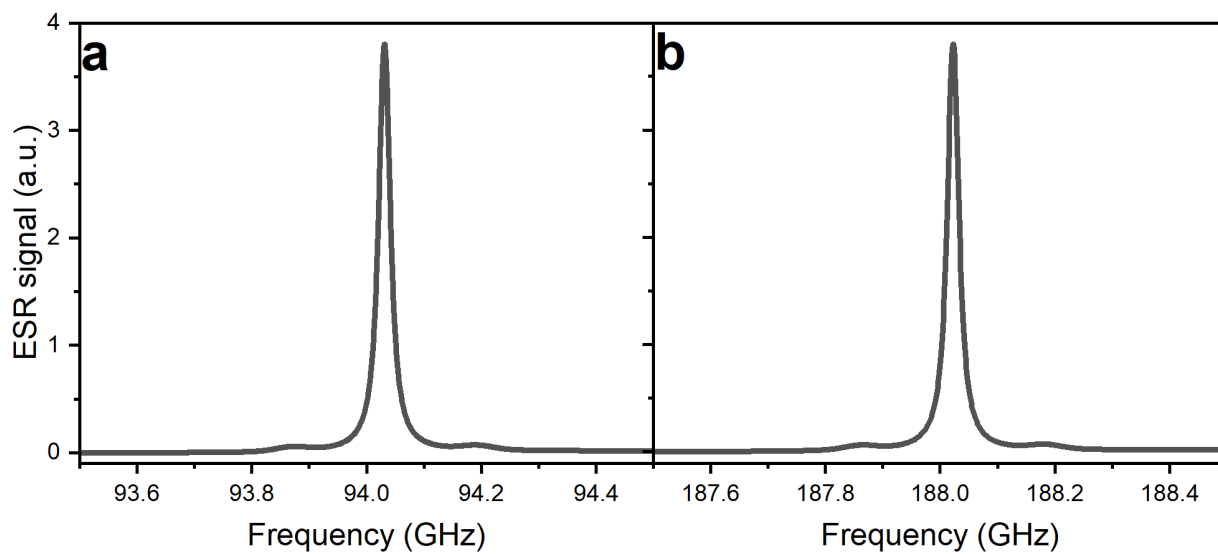


Figure S8: Simulation of ESR spectra for P sample at 3.3451 T (a) and at 6.6919 T (b). Simulation has been done using EasySpin after the best (111) P_b and P_b^{iso} system was obtained from fitting of the experimental ESR data (Fig. S4). The magnetic field values were calculated from the spectrometer frequency.

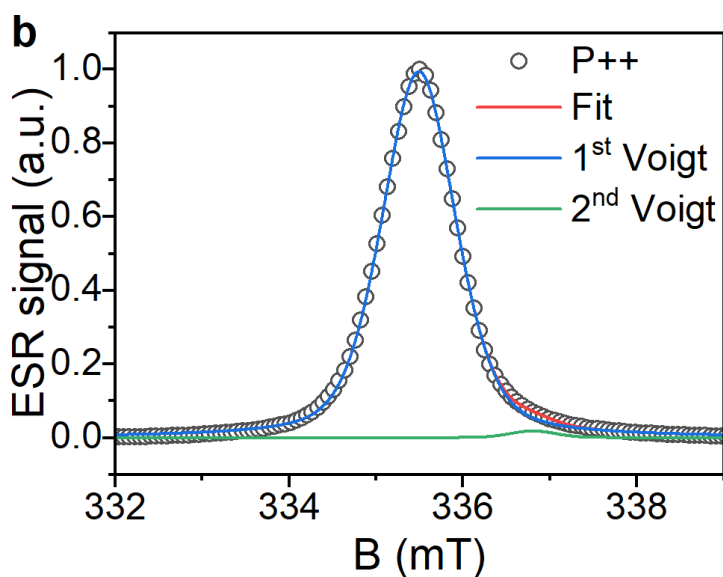


Figure S9: Fitting of the ESR spectrum of P++ PSi NPs with two pseudo-Voigt lines (red line). The first and second Voigt lines give g -factors of 2.0054 and 1.9991, respectively. The ESR spectrum was obtained by integrating the corresponding ESR spectrum. The FWHM for $g = 1.9991$ peak is 0.4 mT.

S3 Dynamic nuclear polarization

S3.1 Thermal polarization buildup

The polarization enhancement and polarization degree was calculated by integrating the pseudo-Voigt fits of FFT-processed FID data. The integrated values were then divided by the thermal polarization signal processed the same way and taken after 72 h of polarization inside a polarizer with microwave radiation switched off (Fig. S10).

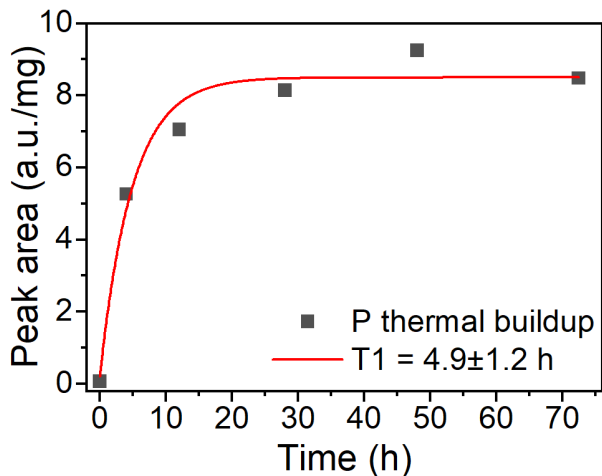


Figure S10: Thermal polarization buildup for the P sample at 6.7 T and 1.4 K.

S3.2 DNP profiles

The normalized DNP profiles (sweep spectra) at 6.7 T and 1.4 K for thermally oxidized PSi NPs are depicted in Fig. S11. There are minor differences between the Si types in the asymmetry of positive and negative peak values. This asymmetry was attributed to the slight difference of surface area induced by increased remote etching for highly doped Si,⁵ and the corresponding possible change in the structure of P_b centers.

In all the spectra, however, the absolute value of the negative peak is smaller than the positive of the peak. The main reason was the non-uniform output power dependence of the microwave generator, which decreased for higher frequencies. When the microwave generator

was upgraded, the typical shape of the sweep curve for DNP with P_b centers was observed (Fig. S12, Fig. S13 N 1LO and N -Au samples). Nevertheless, most of the data was obtained with the old microwave generator, and, therefore, the positive peak was selected to study buildup, in agreement with our data at 3.4 T. Almost complete absence of the negative peak for N++ PSi NPs can at least partially be attributed to its generally low polarization.

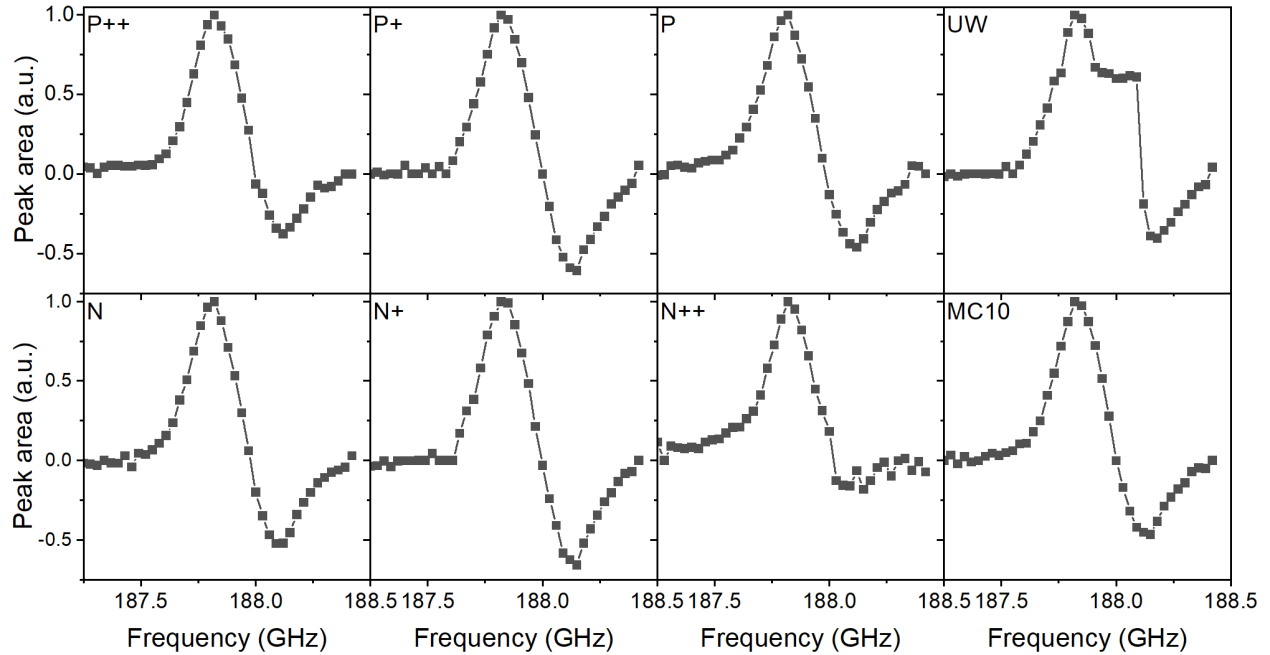


Figure S11: Microwave sweep spectra for thermally oxidized samples of different doping types at 6.7 T and 1.4 K. Each point of a spectrum includes microwave modulation with a frequency of 3 kHz and bandwidth of 150 MHz.^{19,20} Significant decrease of amplitude of the negative peak can be due to decrease of the microwave power with the increase of frequency.

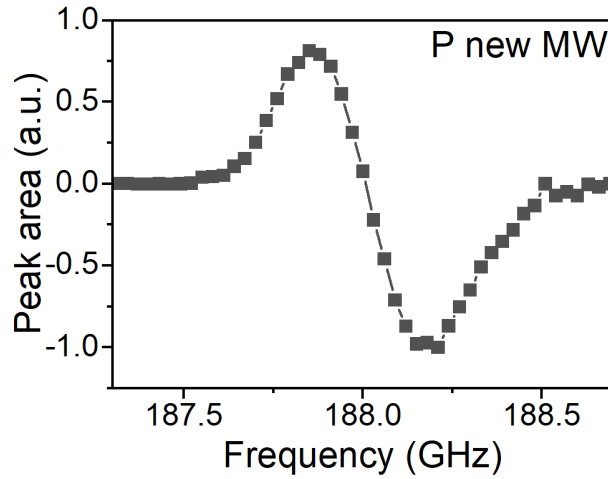


Figure S12: Microwave sweep spectrum of P PSi NPs at 6.7 T and 1.4 K after replacement of microwave generator. The spectrum shows typical asymmetry for DNP of Si using P_b centers.¹⁹⁻²¹

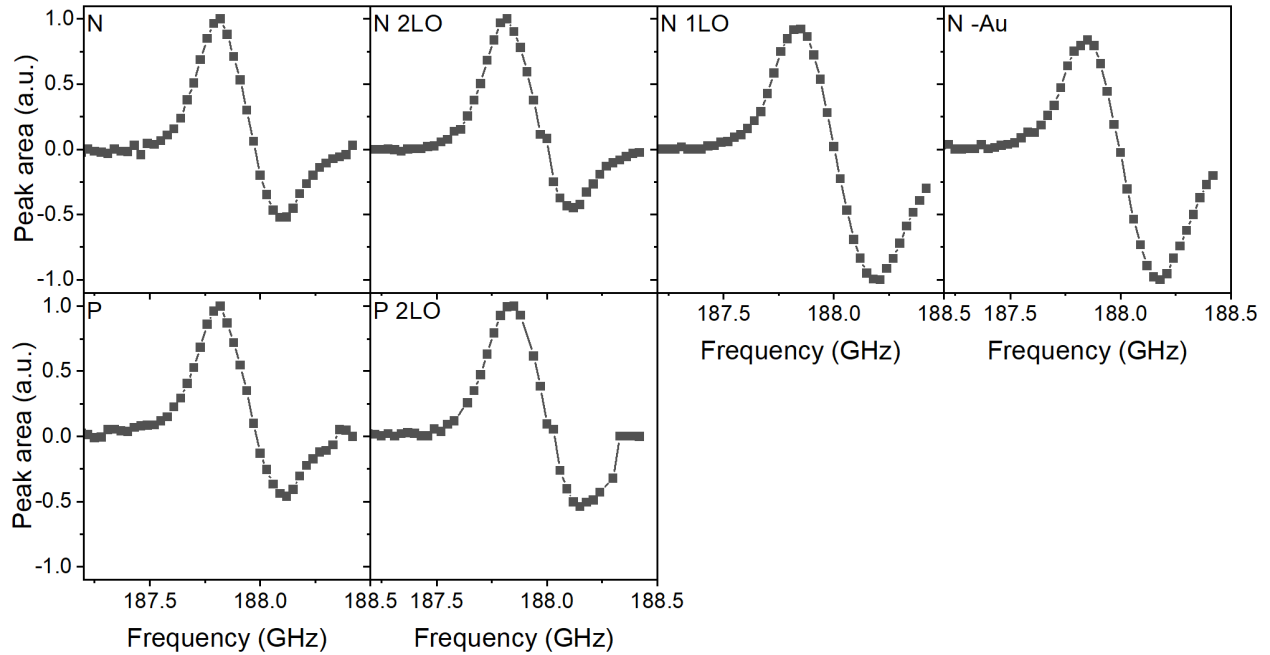


Figure S13: Microwave sweep spectra for differently oxidized N and P PSi NPs at 6.7 T and 1.4 K. Each point of a spectrum includes microwave modulation with a frequency of 3 kHz and bandwidth of 300 MHz.^{19,20}

S3.3 Dynamic nuclear polarization

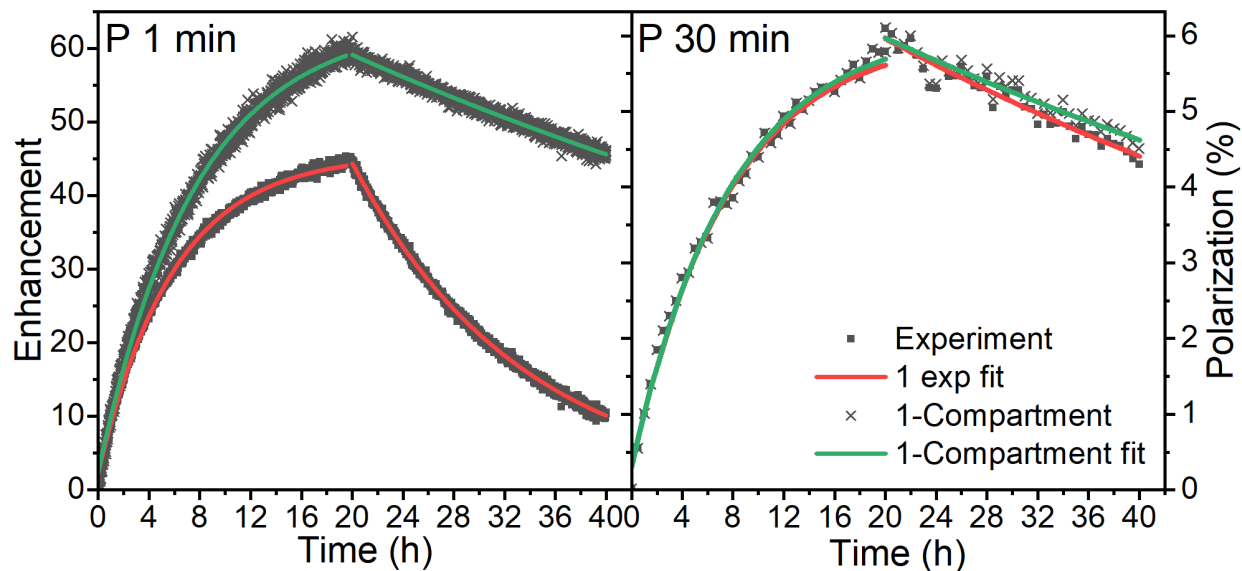


Figure S14: Evaluation of the RF pulse correction and one-compartment model using different sampling rate for the P PSi NPs sample: NMR measurement each 1 min (left) and each 30 min (right) with flip angle $\sim 3^\circ$. The RF pulse correction accurately predicts the polarization buildup and decay for the high sampling rate compared to the low sampling rate provided that NMR flip angle was correctly estimated.

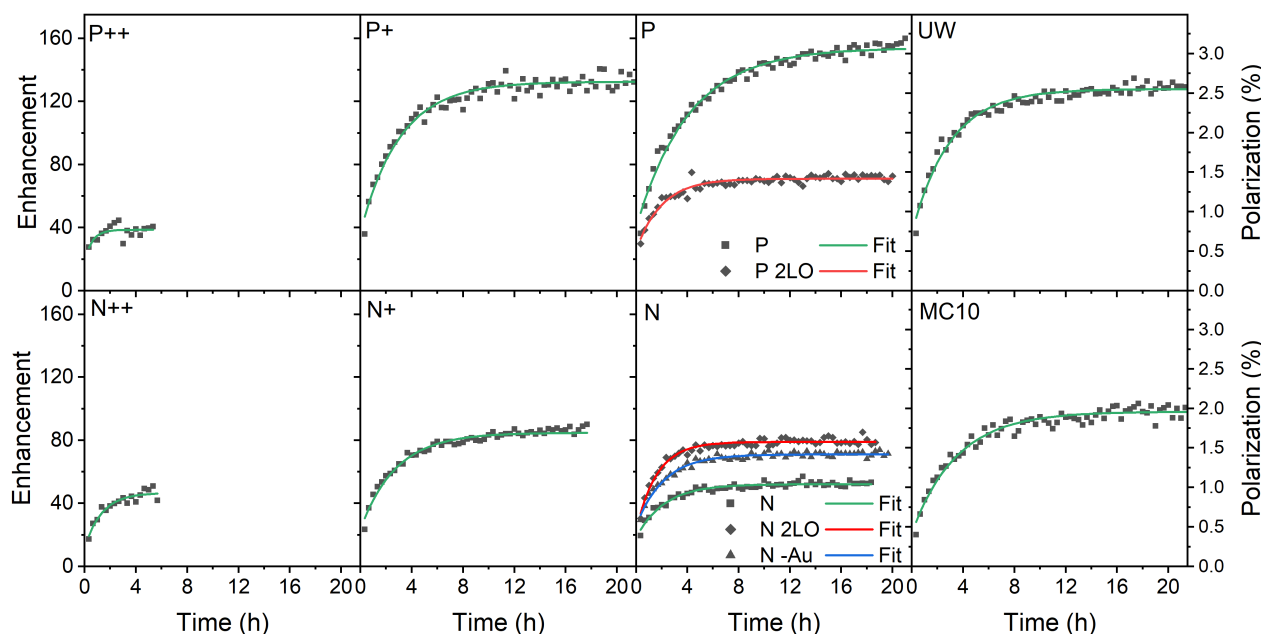


Figure S15: Dynamic nuclear polarization of thermally oxidized PSi NPs with different dopants (dark squares) and single exponential fit with RF pulse correction according to the one-compartment model²² (green lines). Magnetic field is 3.34 T, temperature is 3.4 K, microwave frequency is 93.83 GHz with around 200 MHz modulation, microwave power is 200 mW.

Table S3: Relaxation time of the selected PSi NPs at various DNP conditions and switched off microwave radiation.

Abbreviation	τ_{dec} , h	
	6.7 T (1.4 K)	7 T (3.4 K)
P++	17.5 ± 0.8	-
P+	21.8 ± 0.8	-
P	76.9 ± 17.9	7.4 ± 0.2
P 2LO	13.6 ± 3.3	-
UW	20.7 ± 2.4	6.8 ± 0.1
N	79.5 ± 48.2	4.2 ± 0.2
N 2LO	12.3 ± 0.4	-
N -Au	-	3.7 ± 0.4
N+	32.9 ± 2.6	-
N++	20.0 ± 7.5	-
MC10	24.8 ± 3.1	-

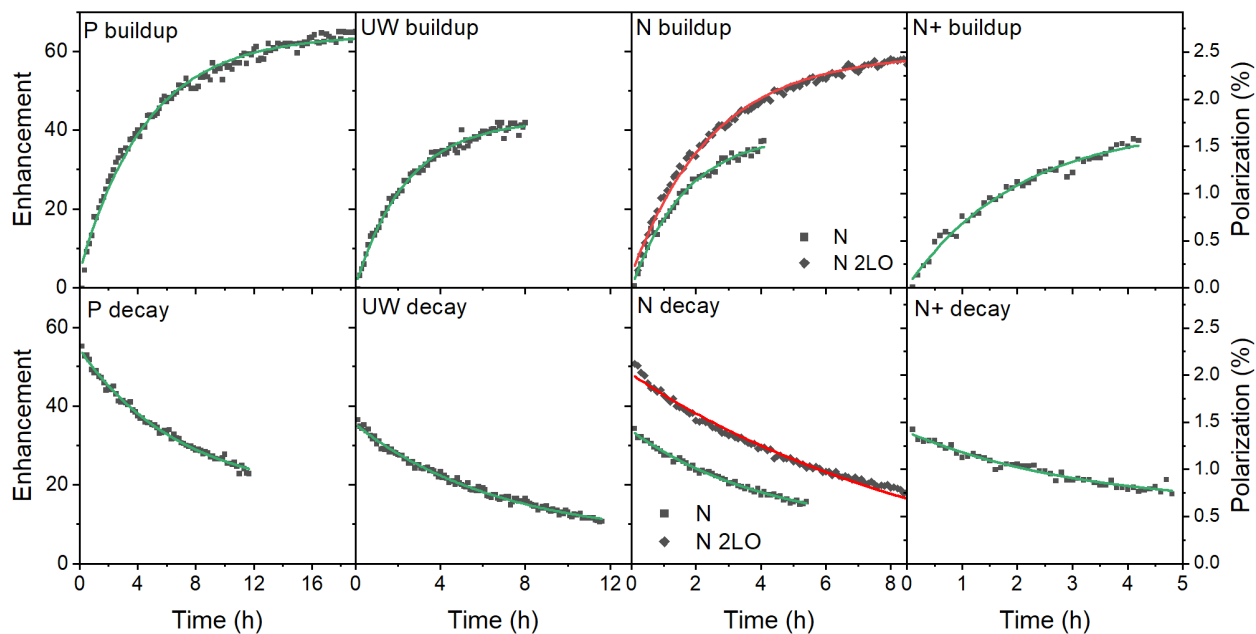


Figure S16: Dynamic nuclear polarization buildup and polarization decay of thermally oxidized PSi NPs with different dopants (dark squares) and single exponential fit with RF pulse correction according to the one-compartment model²² (green lines). Magnetic field is 7 T, temperature is 3.4 K. The buildup microwave frequency is 197.025 GHz with 300 MHz modulation, microwave power is 200 mW.

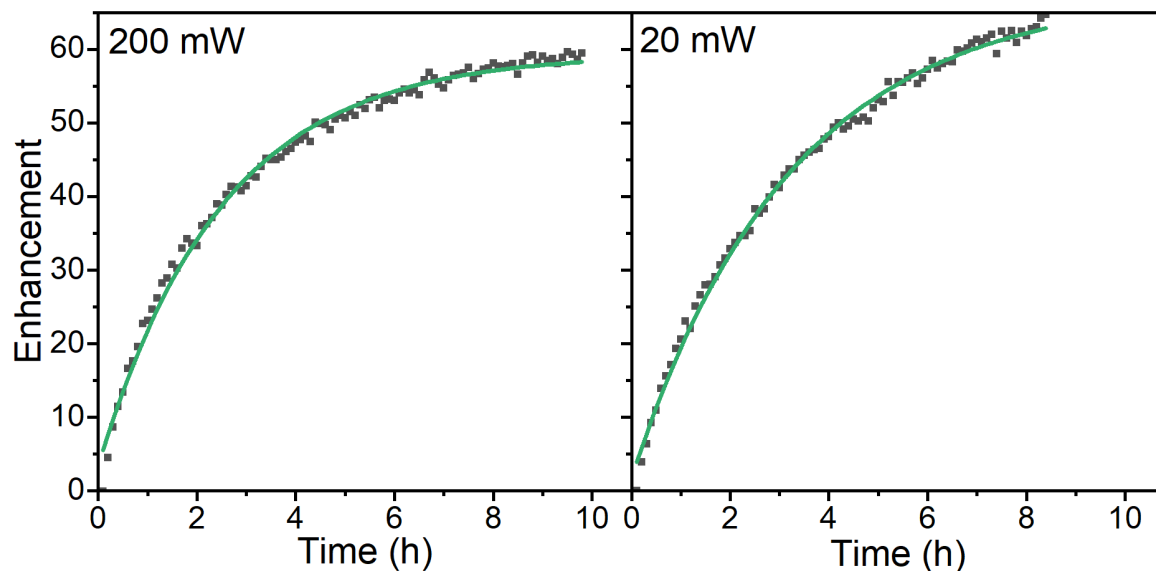


Figure S17: Microwave power dependence of the ^{29}Si polarization buildup at 7 T (3.4 K). The microwave powers were 200 mW (left) and 20 mW (right). The N 2LO sample was used. The DNP buildup times calculated using the one-compartment model were 2.6 ± 0.1 h and 3.4 ± 0.1 h for the 200 mW and 20 mW power, respectively. $k_W = 10.7 \cdot 10^{-3} \text{ h}^{-1}$ and $8.9 \cdot 10^{-3} \text{ h}^{-1}$; $k_R^{\text{bup}} = 0.44 \text{ h}^{-1}$ and 0.36 h^{-1} for 200 mW and 20 mW, respectively.

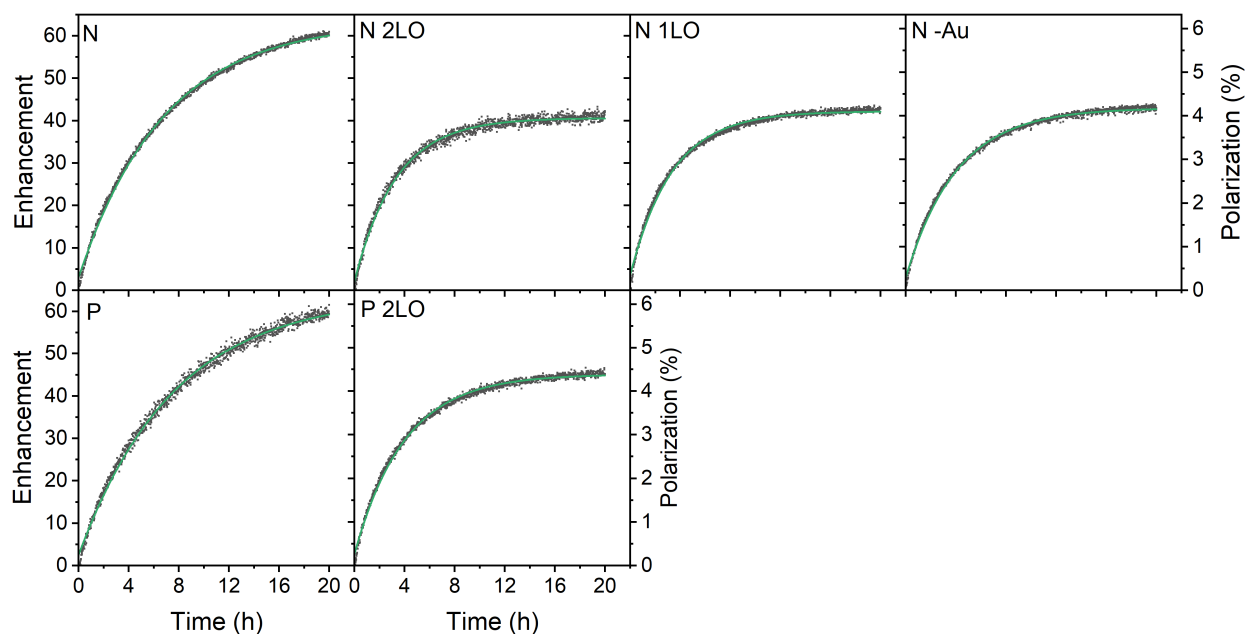


Figure S18: Dynamic nuclear polarization of differently oxidized N and P PSi NPs (dark squares) and single exponential fit with RF pulse correction according to the one-compartment model²² (green lines). Magnetic field is 6.7 T, temperature is 1.4 K, microwave frequency is 187.82 GHz with 200 MHz modulation, microwave power is 30 mW.

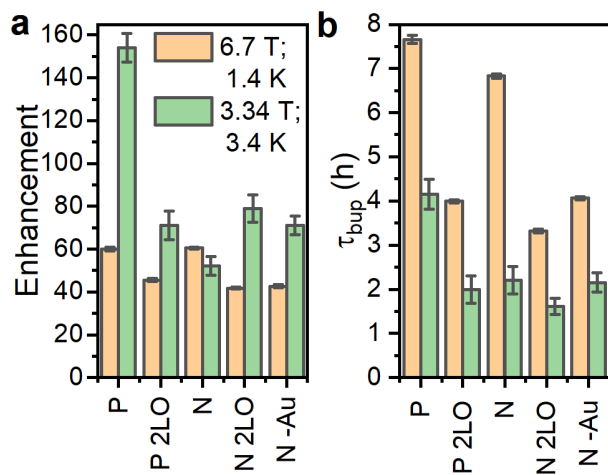


Figure S19: Oxidation induced change of the enhancement (a) and buildup time (b) for the P and N samples at 6.7 T (1.4 K) (orange bars) and 3.34 T (3.4 K) (green bars). The 2LO demotes the two-step liquid oxidation applied after the thermal oxidation either to P or to N sample (Section S1). The N -Au sample is the N sample with dissolved Au NPs after LL-MACE, for which the dissolution medium performed the surface oxidation (no thermal oxidation applied).

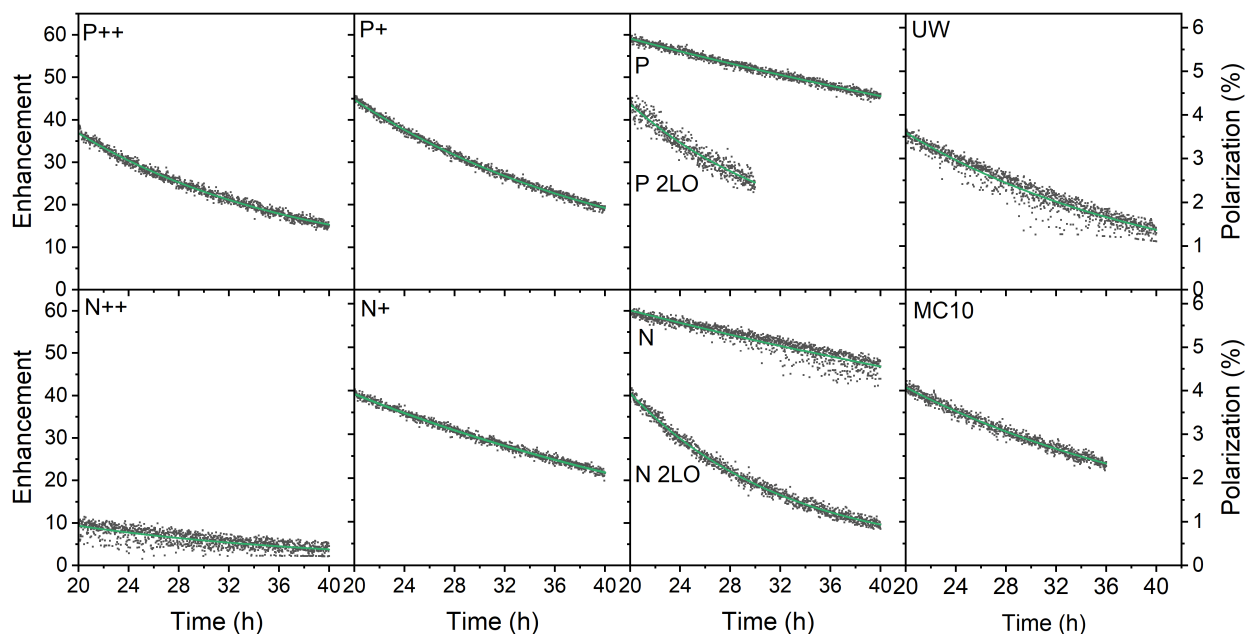


Figure S20: Relaxation of the ^{29}Si polarization for different PSi NPs (dark squares) at the DNP conditions (6.7 T and 1.4 K). Single exponential fits (green lines) with RF pulse correction are according to the one-compartment model.

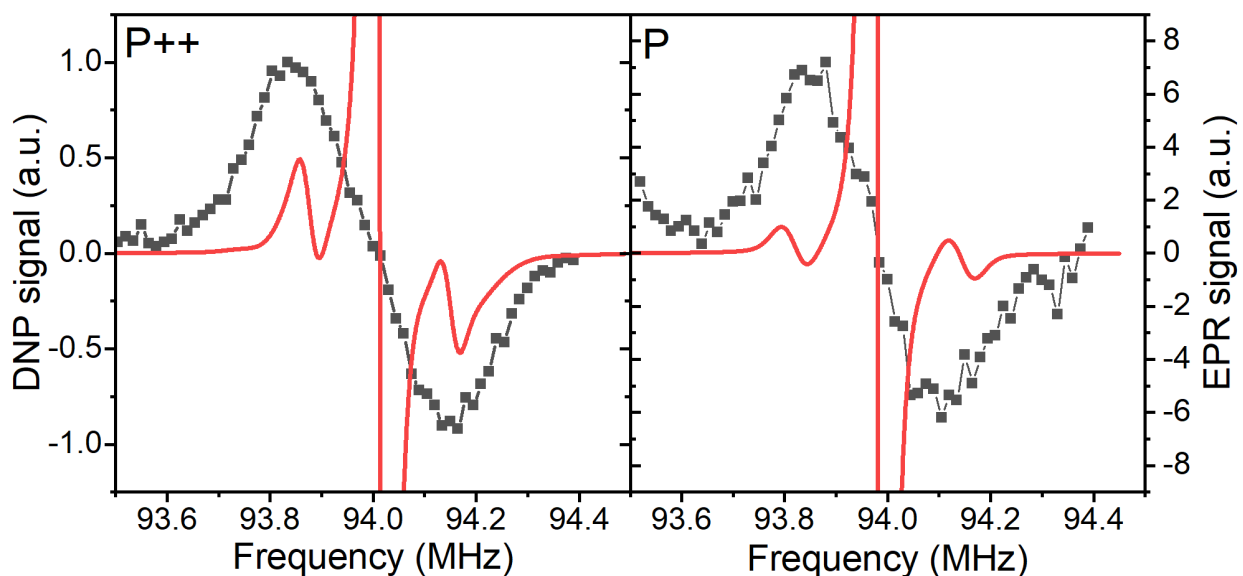


Figure S21: The sweep spectra overlapped with the simulated ESR spectra for P++ and P PSi NPs at 3.35 T and 1.6 K. The sweep was recorded with 100 MHz frequency modulation, 1 kHz sweep rate and 80 mW power.

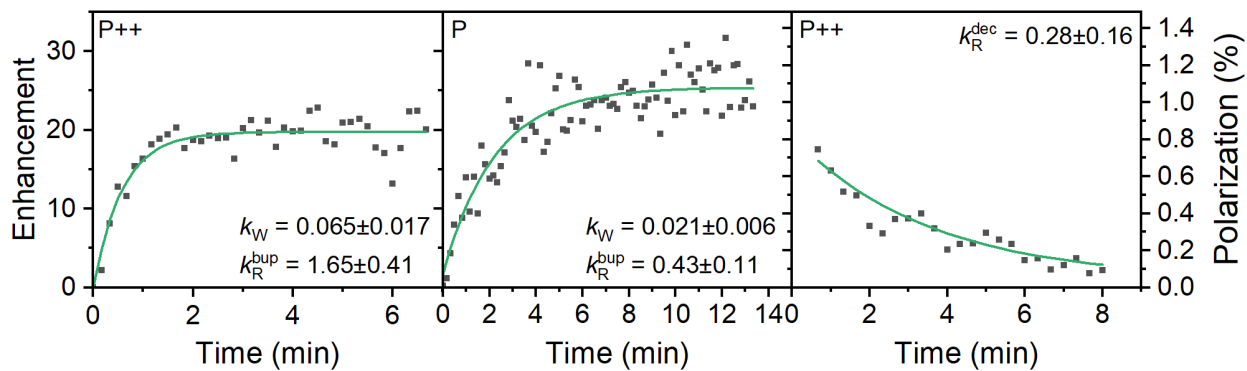


Figure S22: The polarization buildups for P++ and P PSi NPs and the polarization for P++ sample. The buildup was performed with 100 MHz frequency modulation, 1 kHz sweep rate and 80 mW power. The calculated rate constants from the one-compartment model are depicted in the graphs.

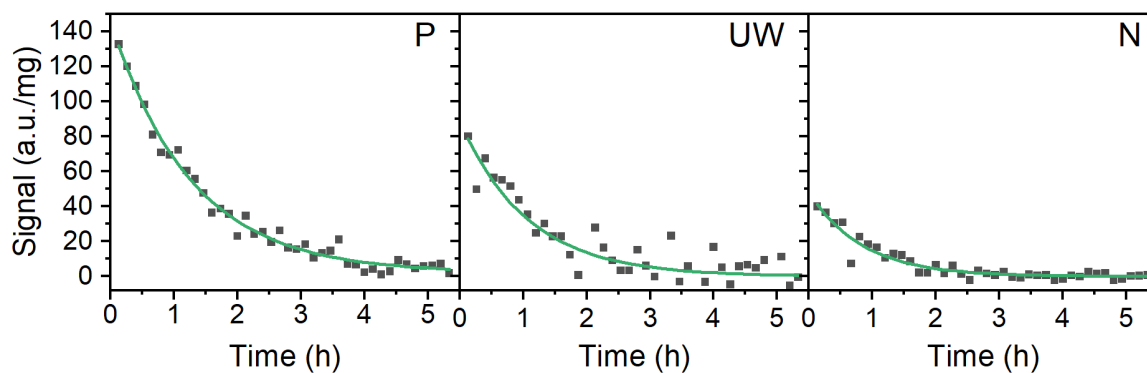


Figure S23: Relaxation of the ^{29}Si polarization for different PSi NPs (dark squares) at 7 T and room temperature (300 K). The decay times are listed in Table ?? in the main text.

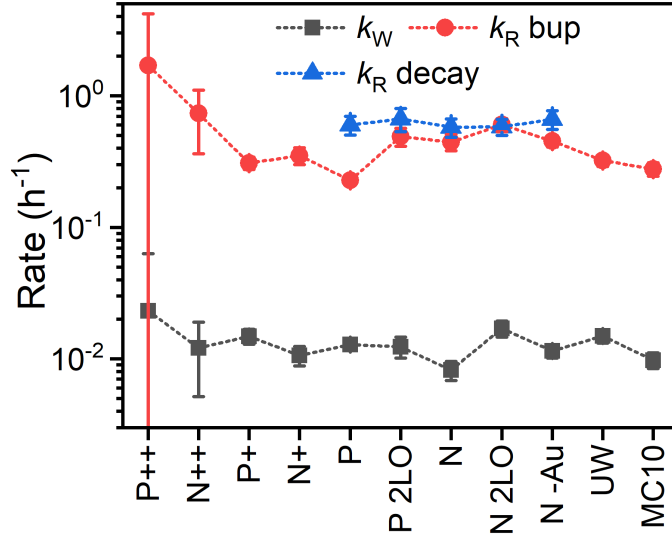


Figure S24: One-compartment model parameters calculated from the polarization build (dark squares and red circles) for the P*Si* NPs with different doping and oxidation. Decays were recorded only for around 5 hours only, resulting in underestimated decay relaxation rates. Magnetic field strength is 3.34 T, temperature is 3.4 K. Lines are guide to the eye.

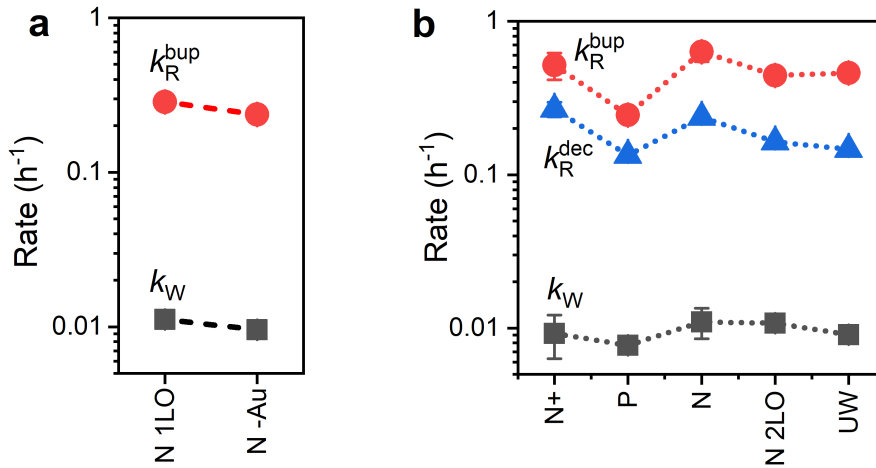


Figure S25: The polarization injection rates k_W and the decay rates during the buildup k_R^{bup} and decay k_R^{dec} . (a) Rates for the N 1LO and N -Au samples at 6.7 T (1.4 K). (b) Rates for the selected samples at 7 T (3.4 K). The rates were extracted from the one-compartment model.²² Lines are guide to the eye.

S4 Density functional theory (DFT) simulations

Spin polarized density functional theory (DFT) simulations to calculate the HF and SHF interaction from first principles were performed with the *CP-PAW* code (<http://www2.pt.tu-clausthal.de/paw/>), employing the projector augmented wave (PAW) approach²³ and Perdew-Burke-Ernzerhof (PBE) exchange functional.²⁴ The plane-wave cutoffs were set to 40 Ry for the wave functions and to 80 Ry for the charge density. The silicon lattice constant was set to 0.5431 nm. The simulation box consisted of five conventional eight-atomic unit cells in each spatial direction, resulting in 1000 lattice sites. A single silicon atom in the centre of unit cell was replaced by either a boron or a phosphorous atom. The isotropic Fermi-contact HF interaction of the P dopant was calculated to 91.1 MHz - in agreement with the experimental value of 117.5 MHz²⁵ considering the finite unit cell of the simulation and PBE functional.²⁶ For the B dopant, the calculated isotropic Fermi-contact HF interaction is 1.4 MHz for an applied strain of 4 kbar as employed in previous DNP experiments.²⁷ The largest computed Si SHF for the P dopant is 7.3 MHz, which is close to the measured 6 MHz.²⁵ The values for the P dopant are more than an order of magnitude larger than the computed 0.5 MHz in the B case.

References

- (1) Riikonen, J.; Salomäki, M.; Van Wonderen, J.; Kemell, M.; Xu, W.; Korhonen, O.; Ritala, M.; MacMillan, F.; Salonen, J.; Lehto, V. P. Surface chemistry, reactivity, and pore structure of porous silicon oxidized by various methods. *Langmuir* **2012**, *28*, 10573–10583.
- (2) Nissinen, T.; Näkki, S.; Laakso, H.; Kučiauskas, D.; Kaupinis, A.; Kettunen, M. I.; Liimatainen, T.; Hyvönen, M.; Valius, M.; Gröhn, O.; Lehto, V. P. Tailored Dual PEGylation of Inorganic Porous Nanocarriers for Extremely Long Blood Circulation in Vivo. *ACS Applied Materials & Interfaces* **2016**, *8*, 32723–32731.

- (3) Xu, W.; Riikonen, J.; Nissinen, T.; Suvanto, M.; Rilla, K.; Li, B.; Wang, Q.; Deng, F.; Lehto, V. P. Amine surface modifications and fluorescent labeling of thermally stabilized mesoporous silicon nanoparticles. *Journal of Physical Chemistry C* **2012**, *116*, 22307–22314.
- (4) Tamarov, K.; Swanson, J. D.; Unger, B. A.; Kolasinski, K. W.; Ernst, A. T.; Aindow, M.; Lehto, V.-P.; Riikonen, J. Controlling the nature of etched Si nanostructures: High versus low load metal-assisted catalytic etching (MACE) of Si powders. *ACS Applied Materials & Interfaces* **2020**, *12*, 4787–4796.
- (5) Tamarov, K.; Kiviluoto, R.; Swanson, J.; Unger, B.; Ernst, A.; Aindow, M.; Riikonen, J.; Lehto, V.-P.; Kolasinski, K. Low-Load Metal-Assisted Catalytic Etching Produces Scalable Porosity in Si Powders. *ACS Applied Materials & Interfaces* **2020**, *12*, 48969–48981.
- (6) Konstantinova, E. A. In *Handbook of Porous Silicon*, 2nd ed.; Canham, L. T., Ed.; Springer International Publishing, 2018; pp 627–654.
- (7) Electron spin resonance features of the Pb1 interface defect in thermal (100)Si/SiO₂. *Materials Science Forum* **1997**, *258-263*, 1713–1718.
- (8) Brower, K. L. Electron paramagnetic resonance studies of Si-SiO₂ interface defects. *Semiconductor Science and Technology* **1989**, *4*, 970–979.
- (9) Stoll, S.; Schweiger, A. EasySpin, a comprehensive software package for spectral simulation and analysis in EPR. *Journal of Magnetic Resonance* **2006**, *178*, 42–55.
- (10) Von Bardeleben, H. J.; Schoisswohl, M.; Cantin, J. L. Electron paramagnetic resonance study of defects in oxidized and nitrided porous Si and Si(1-x)Ge(x). *Colloids and Surfaces A: Physicochemical and Engineering Aspects* **1996**, *115*, 277–289.

- (11) Nissinen, T.; Ikonen, T.; Lama, M.; Riikonen, J.; Lehto, V.-P. Improved production efficiency of mesoporous silicon nanoparticles by pulsed electrochemical etching. *Powder Technology* **2016**, *288*, 360–365.
- (12) Stesmans, A.; Afanas'ev, V. V. Electron spin resonance features of interface defects in thermal (100) Si/SiO₂. *Journal of Applied Physics* **1998**, *83*, 2449–2457.
- (13) Stesmans, A.; Van Gorp, G. Observation of dipolar interactions between Pb0 defects at the (111) Si/SiO₂ interface. *Physical Review B* **1990**, *42*, 3765–3768.
- (14) Gorp, V.; Stesmans, A. Dipolar interaction between [111] Pb defects at the (111)Si/SiO₂ interface revealed by electron-spin resonance. *Physical Review B* **1992**, *45*, 4344–4371.
- (15) Meyer, B. K.; Petrova-Koch, V.; Muschik, T.; Linke, H.; Omling, P.; Lehmann, V. Electron spin resonance investigations of oxidized porous silicon. *Applied Physics Letters* **1993**, *63*, 1930–1932.
- (16) Himmler, A.; Albannay, M. M.; Von Witte, G.; Kozerke, S.; Ernst, M. Electroplated waveguides to enhance DNP and EPR spectra of silicon and diamond particles. *Magnetic Resonance* **2022**, *3*, 203–209.
- (17) Young, C. F.; Poindexter, E. H.; Gerardi, G. J. Electron paramagnetic resonance of porous silicon : Observation and identification of conduction-band electrons. *Journal of Applied Physics* **1997**, *81*, 7468–7470.
- (18) Young, C.; Poindexter, E.; Gerardi, G. Electron paramagnetic resonance of conduction-band electrons in silicon. *Physical Review B* **1997**, *55*, 16245–16248.
- (19) Kwiatkowski, G.; Jähnig, F.; Steinhauser, J.; Wespi, P.; Ernst, M.; Kozerke, S. Nanometer size silicon particles for hyperpolarized MRI. *Scientific Reports* **2017**, *7*, 7946.
- (20) Kwiatkowski, G.; Polyhach, Y.; Jähnig, F.; Shiroka, T.; Starsich, F. H. L.; Ernst, M.; Kozerke, S. Exploiting Endogenous Surface Defects for Dynamic Nuclear Polarization

- of Silicon Micro- and Nanoparticles. *The Journal of Physical Chemistry C* **2018**, *122*, 25668–25680.
- (21) Dementyev, A. E.; Cory, D. G.; Ramanathan, C. Dynamic Nuclear Polarization in Silicon Microparticles. *Physical Review Letters* **2008**, *100*, 127601.
- (22) Witte, G. V.; Ernst, M.; Kozerke, S. Modelling and correcting the impact of RF pulses for continuous monitoring of hyperpolarized NMR. *Magnetic Resonance* **2023**, 1–16.
- (23) Blöchl, P. E. Projector augmented-wave method. *Physical Review B* **1994**, *50*, 17953–17979.
- (24) Perdew, J. P.; Ernzerhof, M.; Burke, K. Rationale for mixing exact exchange with density functional approximations. *Journal of Chemical Physics* **1996**, *105*, 9982–9985.
- (25) Feher, G. Electron spin resonance experiments on donors in silicon. I. Electronic structure of donors by the electron nuclear double resonance technique. *Physical Review* **1959**, *114*, 1219–1244.
- (26) Swift, M. W.; Peelaers, H.; Mu, S.; Morton, J. J.; Van de Walle, C. G. First-principles calculations of hyperfine interaction, binding energy, and quadrupole coupling for shallow donors in silicon. *npj Computational Materials* **2020**, *6*, 1–9.
- (27) Henstra, A.; Dirksen, P.; Wenckebach, W. T. Enhanced dynamic nuclear polarization by the integrated solid effect. *Physics Letters A* **1988**, *134*, 134–136.